



# Ultrasonic SH guided wave detection of the defects of switch rails with 3D finite element method

Xiafei Li<sup>a</sup>, Bin Wu<sup>b</sup>, Xiang Gao<sup>b,\*</sup>, Yao Liu<sup>a</sup>, Huan Wang<sup>a</sup>, Xiucheng Liu<sup>b</sup>

<sup>a</sup> Faculty of Materials and Manufacturing, Beijing University of Technology, Beijing, PR China

<sup>b</sup> Faculty of Information Technology, Beijing University of Technology, Beijing, PR China

## ARTICLE INFO

### Keywords:

Ultrasonic SH guided wave  
Switch rail  
Defect detection  
3D finite element method  
Grid

## ABSTRACT

A switch rail is an important part of the high-speed railway system, but it is highly susceptible to defects during service, which threaten traffic safety. A switch rail has an asymmetric variable cross-section structure, which makes it challenging to detect its defects with ultrasonic testing. In this study, the finite element model of switch rails and the ultrasonic SH guided wave detection of groove defects were explored. The three-dimensional finite element model of switch rails with the same sizes used under working conditions was established. Furthermore, the influences of grid division method, switch mechanism setting method, and root end variable cross-section grid type on guided wave propagation in the model were analyzed in detail. The switch rail model was experimentally validated. The ultrasonic SH guided wave detection of the defects at the rail head and rail bottom was successfully realized and the echo signals from other special structures of switch rail were also obtained. The finite element model calibrated with experimental results could be used to simulate guided wave detection at any location with any defect. The calibrated model could optimize the switch rail guided wave detection scheme and guide signal identification. The study provides an important basis for the inspection and monitoring of switch rails.

## 1. Introduction

High-speed railways are a crucial component of modern infrastructure and play a vital role in efficient transportation [1]. As a crucial part of the railway system, the turnout is an essential piece of rail equipment for a locomotive turning from one rail to another and involves the weak points of rail structures [2]. As the main component of the turnout, a switch rail directly bears the weight of the wheel pair and faults and injuries may be generated in the service life and impair its serviceability and traffic safety [3,4]. In the actual operation, a switch rail is vulnerable to local cracking due to complex load conditions and large-deformation cycles. Once a crack expands, it easily causes safety incidents, such as a rail failure [5,6]. In the current rail inspection technology, ultrasonic waves are mainly used to scan rails, but crucial parts of rails such as switch rail were seldom explored with ultrasonic waves [7], because the complex variable cross-sectional structure of a switch rail, compared to rail bottom, results in unclear propagation characteristics of ultrasonic guided waves. Particularly, the switch system is not allowed to be dismantled in an in-service inspection, thus resulting in lower detection accuracy. The detection of switch rails has become a

major challenge in the field of railway inspection [8,9].

Ultrasonic guided waves have significant advantages over traditional ultrasonic waves, including long propagation distance and high detection accuracy [10]. The health monitoring of rails have been extensively concerned [11]. Guided waves are widely used in railway detection [12]. In the detection, sensors are arranged around rail head [13], rail web [14–15], and rail bottom [16]. Most of the used guided waves are lamb waves excited by piezoelectric transducers [17,18]. Wu J J et al [19] used piezoelectric sensors installed at two locations of the rail web and rail bottom of the switch rail to excite guided waves to monitor the groove defects at the rail bottom and rail web. However, the dispersion and mode conversion characteristics of lamb waves make echo signals complex and increase the detection difficulty. Non-dispersive SH(shear horizontal)-mode guided waves are more suitable for rail inspection. Rose et al. [20] experimentally evaluated the ability of Lamb waves and SH guided waves to detect rail bottom damages and proved that SH guided waves were more suitable for detecting rail defects. SH guided waves can be used to detect the damage of switch rail bottom and monitor the state of switch rails [21,22,23]. Sun [24] proposed a new oblique incidence point focusing SH EMAT structure, and achieved high

\* Corresponding author.

E-mail addresses: [wb@bjut.edu.cn](mailto:wb@bjut.edu.cn) (B. Wu), [gaoxiang@bjut.edu.cn](mailto:gaoxiang@bjut.edu.cn) (X. Gao), [wanghuana@emails.bjut.edu.cn](mailto:wanghuana@emails.bjut.edu.cn) (H. Wang), [xiuchliu@bjut.edu.cn](mailto:xiuchliu@bjut.edu.cn) (X. Liu).

sensitivity detection of defects in the focusing region. However, the above studies mainly focused on the detection of ordinary rails, but the detection method of switch rails were seldom explored. Unlike the waveguide structures with regular geometric shapes such as pipes, rods, and plates, a switch rail is an acoustic waveguide structure with a complex geometric shape composed of an inverted H-shaped cross-section. The application of guided waves in the detection of rail defects is still difficult.

Due to the particular structure of switch rails, it is difficult to study the propagation characteristics of ultrasonic guided waves in switch rails with analytical methods [25]. When the ultrasonic guided wave propagates in a switch rail, it is affected by rail bottom fastener, switch mechanism, and various connecting plates [26], thus increasing the difficulty in signal analysis. Current studies on guided wave detection of rails and switch rails were mainly carried out through FE (finite element) analysis and experiments. Based on FE analysis results, with the reflected-echo method, the team in Imperial University of Technology adopted a piezoelectric wafer array probe to excite guided waves of different modes in the rail for detecting the artificial defects in rail head and rail bottom and experimentally confirmed that the defects of rail head, rail web, and rail bottom could be well positioned under corresponding excitation modes [27]. Wilcox et al. detected welded joints by means of mode transformation feature maps and found that the results of FE simulation and experimental tests were basically the same [28]. Yuan et al. established a 3D (three-dimensional) transient FE model for high-speed pulsed eddy current testing of rails with cracks, explored the influence of detection speed on detection signals and determined the quantitative characterization method of cracks in high speed motion [29]. Sanderson R and Smith S. analyzed the propagation characteristics of guided waves in rails with the 3D FE model of rails and calculated the dispersion curve of guided waves [30]. Gharaibeh et al. selected eight guided wave modes suitable for detecting rail head, rail web, and rail bottom [31]. FE method plays an important role in the selection of the mode and frequency of guided waves, sensor arrangement way, and detection range. 3D FE method has become the main means to study rail defect detection.

The finite element method has a wide application and can be used for acoustic or mechanical analyses of more complex structures, including numerical simulation of weld areas [32], studies on the overall flow characteristics of aircraft wings [33], and measurements of seismic waves [34]. It is feasible to create a dynamic numerical simulation mechanism in fluid mechanics fluid parameters and pipeline trajectory [35]. The solution of some characteristic parameters associated with flaws can be achieved by studying the characteristics of defects in structures with the finite element method [36]. Some characteristics or phenomena can be predicted, such as the attenuation characteristics of seismic waves [37], mechanical surface adhesive durability [38] and gas flow uniformity [39]. The numerical simulation method is more significant in many fields.

Most researchers carried out local modelling of rails in FE software and explored the propagation characteristics of ultrasonic guided waves in rails and the interaction between guided waves and defects [40]. However, simulation modelling of actual switch rails under working conditions was not investigated. The defects of a switch rail are mainly distributed at rail head, rail web, and rail bottom [41]. A small number of teams established a partial model of rail head to detect the defects in rail head. G. Zumpano [42] investigated the localization of defects with a finite element model and indicated that the localization accuracy of defects was affected by the selected excitation frequency. In order to detect the defects of different shapes and depths in the rail head area with guided waves at 20 kHz and 45 kHz. Bartoli [43] performed a computational analysis of guided wave propagation in rails with commercial finite element software and found that the defect echo amplitude was strengthened as the cross-sectional loss rate increased. Similarly, in a control experiment, when an impact drop hammer was used to excite guided waves in the rail, circumferential damage with a

cross-sectional loss rate of about 15% was detected and the consistency between simulation results and experimental results proved the correctness of the finite element model. A certain team simulated rail bottom to locate the defects at rail bottom. Hu [44] performed in-situ rapid detection of cracks in the rail bottom of pointed rails with ultrasonic B-scan imaging. However, these models were incomplete and the ultrasonic evaluation of the whole rail has not been realized. In previous studies, local models were used to investigate the dispersion curve, signal energy focusing problem, and the optimal excitation frequency and excitation angle of guided waves in different parts and the whole switch rail was mapped based on partial switch rail models. In order to simulate the model more precisely, Haysahi [45] established a simplified model of an integral switch rail in a free state, Setshedi [46] simplified various parts of the switch rail such as rail head, rail web, and rail bottom were simplified into flat structures with different thicknesses so as to investigate the propagation characteristics of guided waves in a switch rail. Switch rails with different cross-sectional shapes and geometric parameters were not well established. In particular, the existing models were established only based on a part of the whole switch rail, so it was not accurate. The rail under the operating state was not in a free state and the propagation of ultrasonic guided waves in the switch rail in a fixed state was affected by various factors such as fastening bolts, fasteners, and switch mechanism. Therefore, multiple scattering characteristics of guided waves at the junction were complex.

This work focused on the ultrasonic guided wave detection of groove defects and the FE modeling approach for switch rails. In order to accurately represent the real functional conditions of a switch rail, a 3D FE model of the same size was firstly established. The effects of the grid division ways of a switch rail and defective parts, the setting method of switch mechanism, and the setting of the root-end variable cross-section grid type on the propagation characteristics of guided wave signals were thoroughly investigated. The correctness of the established switch rail model was experimentally validated and ultrasonic guided wave detection of the defects at switch rail head and rail bottom was successfully realized (Fig. 1). This model allowed the accurate positioning of defects at any location and the acquisition of echo signals from other special structures on the switch and provided the basis for the inspection and monitoring of switch rails in service. The finite element model calibrated with experimental results can be used to simulate guided wave detection at any location with any defect. The calibrated model could optimize the switch rail guided wave detection scheme and guide signal identification.

## 2. Switch rail defect detection experiment and setting of finite element model

### 2.1. Experimental setting

In the experiment, a switch rail with a total length of about 14.28 m was tested. The side near the tip of the switch rail was selected for defect detection. The installation position of the sensor and defect machining locations are shown in Fig. 2(a). The self-developed MsTGW-II (Magnetostrictive Guided-wave Generation System) was used to carry out detection experiments. The system was mainly composed of a computer, a flat-plate magnetostrictive sensor, and an ultrasonic guided-wave detection instrument (Fig. 2(b)). Due to the limitations under actual working conditions, the flat-plate magnetostrictive sensor was mounted at the bottom of the switch rail. The sensor was designed based on the inverse Weidmann effect (Fig. 2(c)).

During the experiment, the signal excitation module output 5-cycle Hanning window-modulated sinusoidal signals, which was amplified by the power amplifier circuit to enter the excitation coil shown in Fig. 2(c) and provide a dynamic magnetic field along the length of the Fe-Co alloy strips. Under the action of a mutually orthogonal biased magnetic field and a dynamic magnetic field, a plane shear stress wave was formed inside the Fe-Co alloy strips. Shear stress wave was coupled to

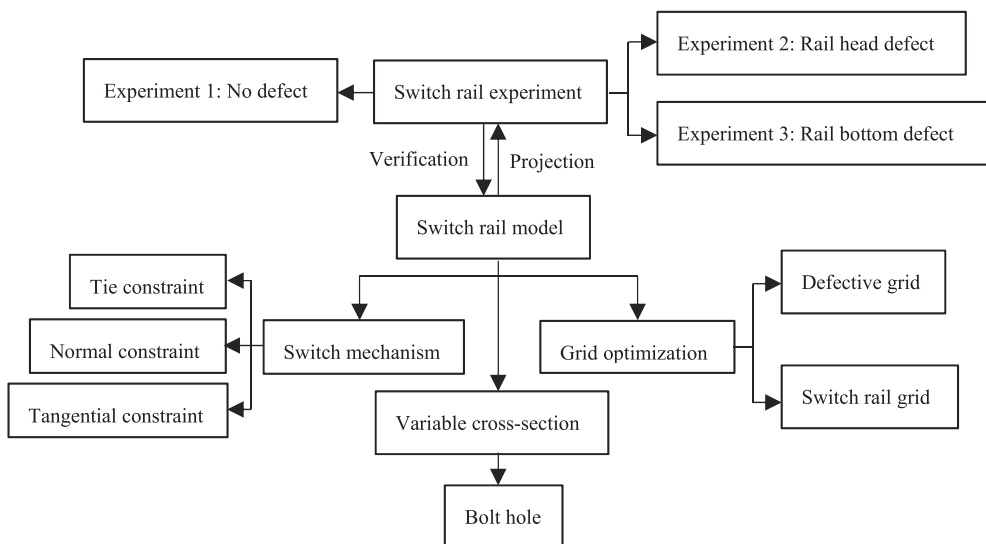


Fig. 1. Research content flow chart.

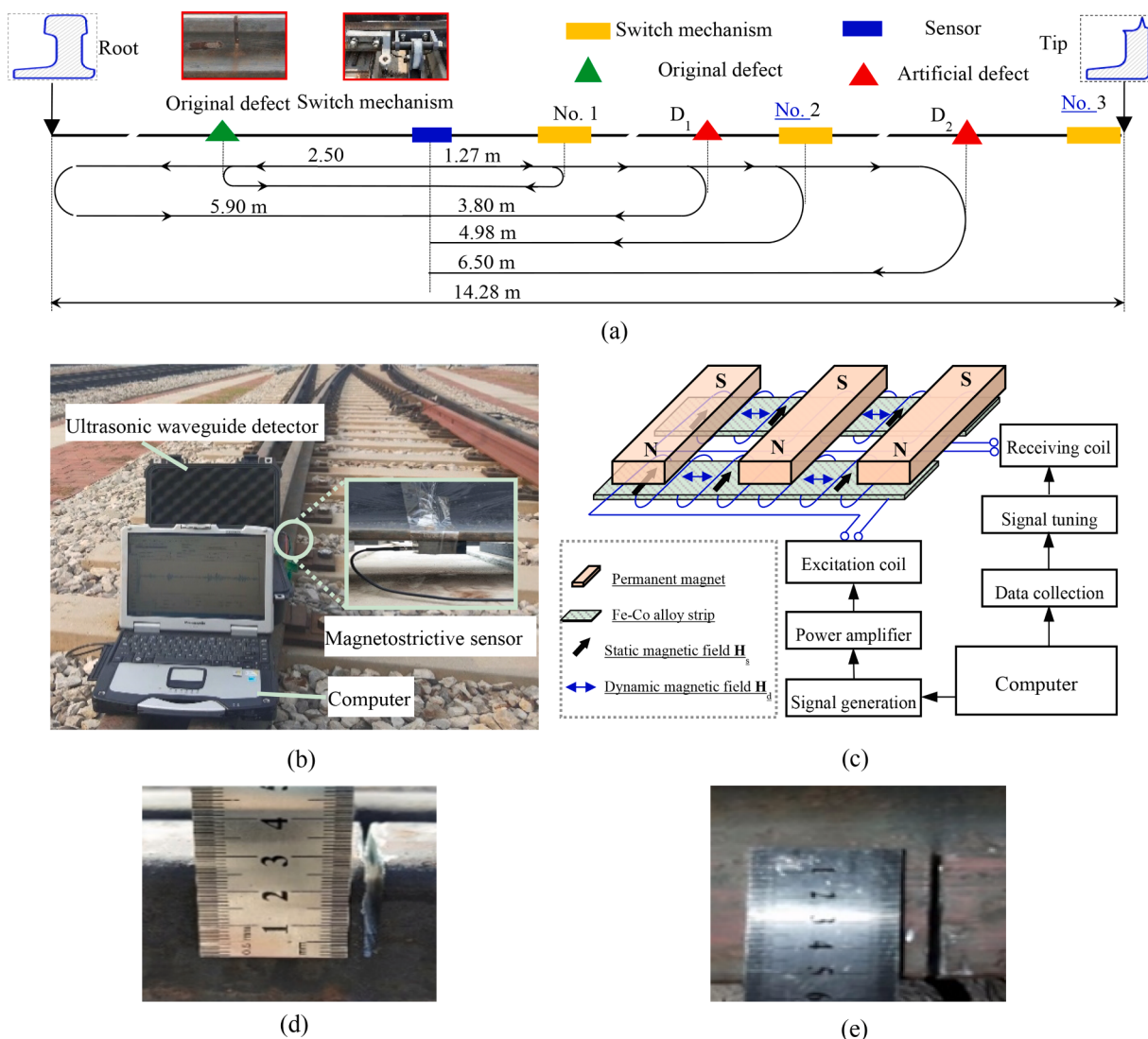


Fig. 2. Sensor installation and defect machining location: (a) diagram of sensor installation position, (b) testing instruments, (c) block diagram, (d) rail head defect, and (e) rail bottom defect.

the bottom of the rail via epoxy resin spread to the cross-section of the switch rail, and propagated along the length of the switch rail to form an ultrasonic guided wave. Guided wave excited by the sensor propagated longitudinally along the switch rail, and its propagation direction was perpendicular to its displacement direction, similar to the propagation direction of SH mode in a plate structure.

The sensor was operated in Pitch-Catch. The central frequencies for guided wave excitation were respectively set to be 30 kHz, 70 kHz, and 100 kHz and the detection experiment was conducted in the following three stages:

- i. In the first stage, the switch rail without defect was tested to acquire five sets of data at each frequency.
- ii. In the second stage, a rail head defect  $D_1$  with the size of  $42.1 \text{ mm} \times 2.0 \text{ mm} \times 24.6 \text{ mm}$  was machined.
- iii. In the third stage, a rail bottom defect  $D_2$  with the size of  $22.7 \text{ mm} \times 2.0 \text{ mm} \times 51.5 \text{ mm}$  was machined.

**Fig. 2(d)-2(e)** show the groove defects machined with an angle grinder. The rail head defect was 3.80 m away from the sensor and the rail bottom defect was 6.50 m away from the sensor.

## 2.2. Setting of the simulation model

The program ABAQUS, an industrial finite element analysis software, offers sophisticated mesh division and analysis tools and can resolve both simple linear issues and complex nonlinear ones. It can solve a variety of physical issues and engineering simulation issues. In order to investigate the influences of the switch rail on the propagation properties of guided waves, in this work, ABAQUS software was used to simulate the switch rail in a scale of 1:1 and examine a few key factors during the modeling process. The simulation process with the FE analysis software ABAQUS involves pre-processing, simulation solution computation, and post-processing. **Fig. 3** depicts its finite element simulation workflow. Here, with ABAQUS, FE simulation was implemented to characterize the propagation characteristics of a bounded ultrasonic beam at the liquid-solid interface.

A 1:1 finite element model of the switch rail was produced in the ABAQUS program in accordance with actual switch rail dimensions (**Fig. 4**). The guided wave excitation position is 5.90 m away from the switch rail root and 8.38 m away from its tip. Three switch mechanisms between the sensor and the end of the switch rail exist. The root end of the pointed rail variable section is composed of a variable section and bolt holes. The defect type, location and depth in the simulation are the same as those in the experiment.

In the simulation, the sensor adopts an excitation-reception model and is set at the bottom of the switch rail. The excitation surface is 50.8 mm wide and covers the bottom of the rail. The excitation signal is set to a 5-cycle sinusoidal signal modulated by Hanning window. The vibration direction of the guided wave is perpendicular to the axial direction of the rail and the guided wave propagates along the axial direction of the rail. In the model, the defect size of rail head and rail bottom is consistent with the defect setting in Section 2.1. The density, Young's modulus, and Poisson's ratio of the switch rail material are 7890 kg/m<sup>3</sup>,

210 GPa, and 0.3, respectively.

The influence of the switch rail overall grid size, the defect part meshing method, the switch mechanism setting method, and the setting of the variable cross-section grid type at the model root end should be further examined to calibrate the switch rail model.

## 3. Finite element model building process

### 3.1. Grid optimization of the FE model of a switch rail

#### 3.1.1. Defect-free switch rail grid optimization

Meshing is a key step in the implementation of FE calculation because the size and type of grids determine the accuracy and efficiency of calculation. To ensure calculation accuracy, the mesh size of the model should be set [47]. According to the wave transmission effect, there are at least 10 cells within one wavelength along the propagation direction:

$$l_e = \frac{1}{10} \frac{\min(V_{ph})}{f} = \frac{\lambda_{\min}}{10} \quad (1)$$

where  $l_e$  is the grid cell length;  $\lambda_{\min}$  is the minimum wavelength;  $V_{ph}$  is the guided wave phase velocity;  $f$  is the center frequency.

The ultrasonic guide wave echo method is used in this paper. The calculated time is from the excitation of ultrasonic guide wave signal to the acquisition of the echo signal of the switch rail end and calculated as follows:

$$T > \frac{2l}{\min(V_g)} \quad (2)$$

where  $T$  is the total time of the analysis step;  $l$  is the length of the model;  $V_g$  is the group velocity of the guided wave.

A switch rail is a complex waveguide structure, so the selection of *ortho*-hexahedral cells generally produces distorted cells and results in meshing failure. When tetrahedral cells or wedge cells are selected, the number of meshes double, thus increasing computing time and decreasing computational efficiency [48]. In summary, we adopted a combined meshing strategy of main hexahedral cells and a small number of wedge cells so as to improve the accuracy of FE calculation and the efficiency of FE modeling.

Taking the guided wave excitation frequency of 30 kHz as an example, the group speed of guided wave propagation is 3260 m/s and the wavelength of the guided wave is 108.67 mm. Therefore, the FE mesh size was selected as one-tenth of the wavelength of excitation signals, 10.87 mm. Considering the computational time and efficiency, we firstly discussed two extreme cases with grid sizes of 2 mm and 10 mm. The switch rail was 14.28 m long and the positioned sensor was 8.38 m away from the switch rail and 5.90 m away from the root end of switch rail (**Fig. 5(a)**).

According to the Pitch-Catch mode, the amplitude and phase of the first end-surface echo were selected as the criteria to assess the grid quality. **Fig. 5(b)** shows the variances in the amplitude and phase of the direct wave at the root end of the switch rail between the grid sizes of 2 mm and 10 mm. The selected grid size accounted for this deviation, indicating that the grid size significantly affected calculation results.

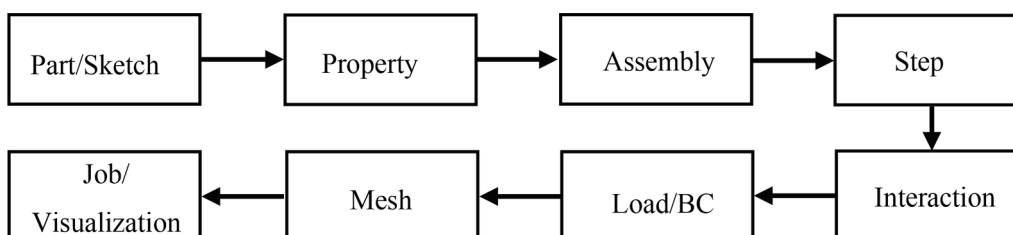


**Fig. 3.** Schematic diagram of the simulation model.

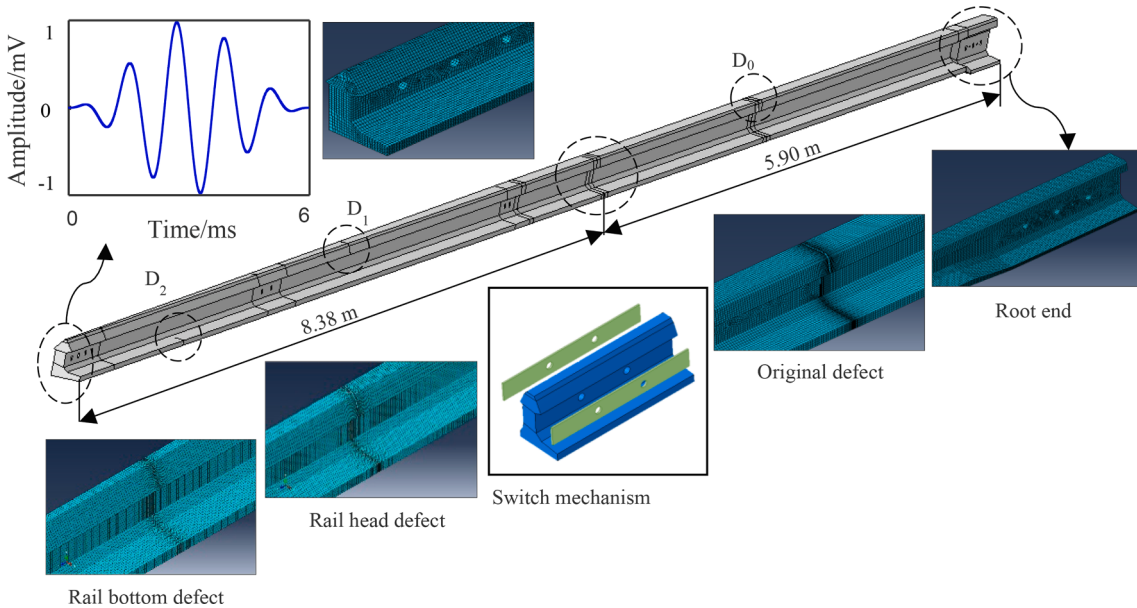


**Fig. 4.** Schematic diagram of the simulation model.

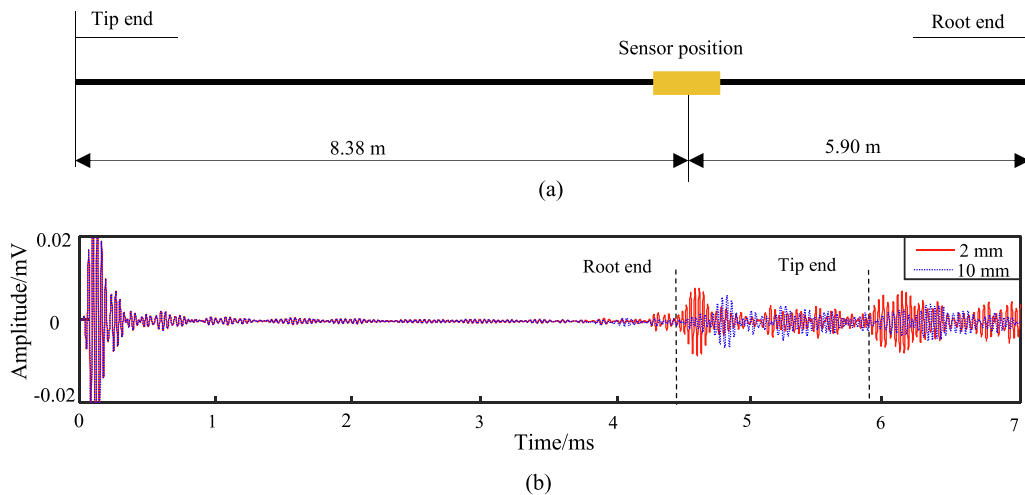


**Fig. 5.** Time domain results under the grid sizes of 2 mm and 10 mm: (a) sensor installation position and (b) time-domain simulation results.

In order to examine the relationship between grid size and the amplitude and phase of echo signal at the root end of switch rail, we counted the number of meshes and gave computation time for hexahedral cells and tetrahedral cells with mesh sizes of 2 mm to 10 mm and an interval of 0.5 mm (**Table 1** and **Table 2**). As the mesh size increased, the numbers and computation time of hexahedral cells and tetrahedral cells gradually decreased and computation time of tetrahedral cells was roughly twice of that of hexahedral cells. As a result, the mesh type of the switch rail model was set to hexahedral cells.

A total of 17 groups of amplitude/phase with grid sizes ranging from 2 mm to 10 mm were calculated in order to achieve the maximum computational accuracy within the shortest time. The effects of grid size

on the amplitude and phase of echo at the end face of the switch rail is shown in **Fig. 6**. As the model grid size increased, the amplitude of end echoes decreased, whereas the phase increased. The amplitude and phase values of the end-surface echoes remained steadily when the grid size increased from 2 mm to 6 mm. The grid size affected the accuracy of numerical solution and thus calculation results. Based on the consideration of calculation time and calculation efficiency, the grid size should be selected in the stable interval.

### 3.1.2. Defective switch rail grid optimization

Typically, increasing defects affected end echoes generated along Path 1, but had little effect on those generated along Path 2. However,

**Table 1**

Relationship between grid size and the quantity and calculation time of tetrahedral elements.

Grid size	2 mm	2.5 mm	3 mm	3.5 mm	...	8.5 mm	9 mm	9.5 mm	10 mm
Quantity	1.5e7	9.9e6	5.2e6	2.4e6	...	7.7e5	5.4e5	4.1e5	2.9e5
Calculation time	13 h	11 h	4 h	1 h	...	0.7 h	0.7 h	0.5 h	0.5 h

h: hour.

**Table 2**

Relationship between grid size and the quantity and calculation time of hexahedral elements.

Grid size	2 mm	2.5 mm	3 mm	3.5 mm	...	8.5 mm	9 mm	9.5 mm	10 mm
Quantity	9.9e6	5.4e6	2.4e6	11.1e6	...	4.1e5	2.5e5	2.0e5	1.5e5
Calculation time	6 h	5 h	2 h	0.5 h	...	0.3 h	0.3 h	0.2 h	0.2 h

h: hour.

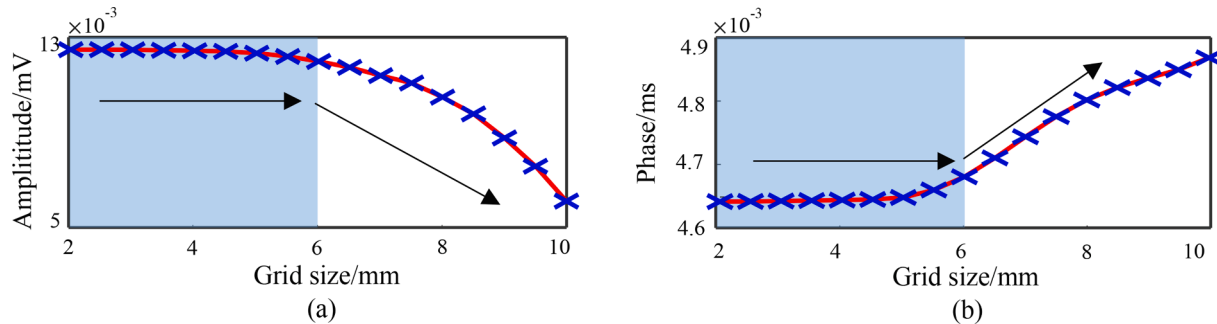


Fig. 6. Influences of grid size on the amplitude and phase of end-face echoes: (a) amplitude and (b) phase.

the variation of grid size affected the amplitude and phase of the echoes at the end face of Path 2. Therefore, it is assumed that the grid division is for this phenomenon.

Fig. 7 shows the comparison of time-domain simulation results of a switch rail with/without defects under a grid size of 2 mm. At the bottom of the switch rail, there was a groove-type defect ( $22 \text{ mm} \times 1 \text{ mm} \times 5 \text{ mm}$ ), which was 4.58 m away from the switch rail and 3.80 m away from the sensor. Under the same grid size, the amplitude and phase of echo signals at the root end of the switch rail with/without defects showed the variances (Fig. 7(c)), thus confirming our assumption. In order to determine the interval segment in which the change in grid size had the least impact on the root-end echoes, we analyzed the amplitude and phase variations between the data at the root end of the switch rail with/without defects.

The amplitude and phase values of the echoes at the root end of switch rails in the defect simulation data under the grid size of 2 mm to 10 mm were recorded (Fig. 8). As the grid size increased, the amplitude of the echo at the root end of the switch rail gradually decreased and the

phase value gradually increased. Under the same grid size, the introduction of defects changed echo amplitude and phase values, indicating that the presence of defects had an impact on calculation accuracy.

The amplitude and phase values of echo signals at the root end of the switch rail with/without defect under the same grid size were analyzed. The differences in the amplitude and phase values of the root-end echo signals of the switch rail with/without defects under the grid size of 2 mm to 10 mm were calculated to obtain corresponding absolute values. The smaller the absolute value was, the smaller the impacts of the grid size on the amplitude and phase of the root-end echo were. Fig. 9 displays the calculation results. As the grid size increased above 5.5 mm, the amplitude difference and phase difference also increased. When the grid size increased from 2 mm to 5.5 mm the amplitude difference and phase value difference were the smallest and remained stable. As a result, we selected a grid size of 2 mm to 5.5 mm as the interval with the least effect on the echoes at the root end.

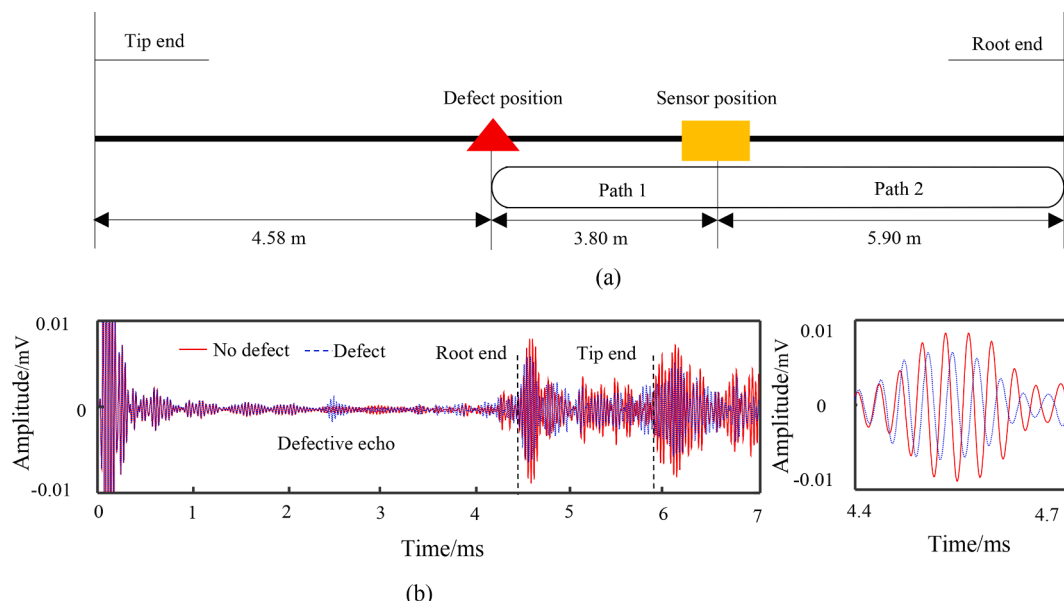
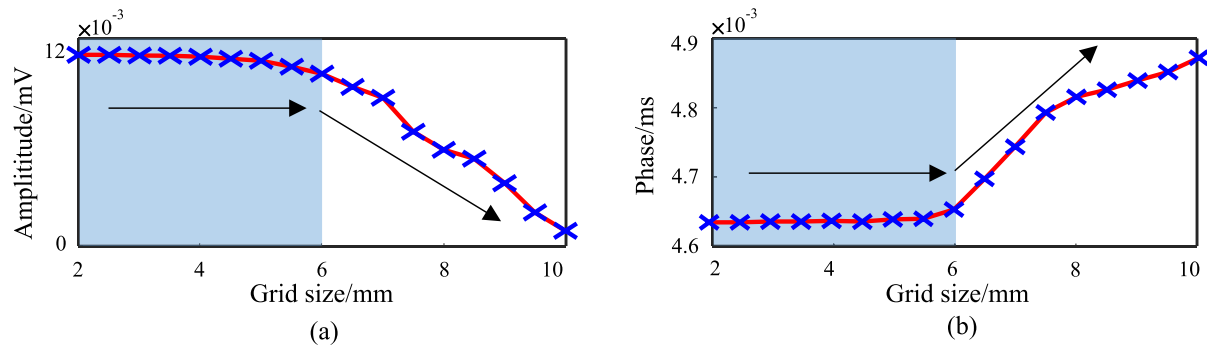
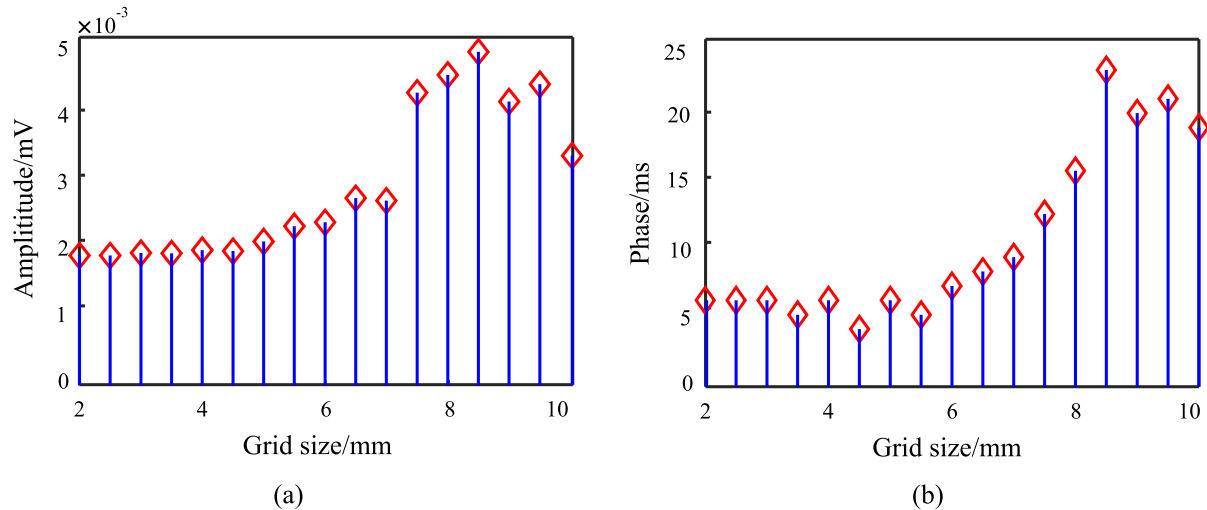


Fig. 7. Comparison diagram of time-domain simulation results with/without defects under the grid size of 2 mm: (a) installation positions of sensors, (b) time-domain simulation results, and (c) enlarged view of the root end of a switch rail.



**Fig. 8.** Impacts of defects on the peak and phase of the root-end echo: (a) amplitude and (b) phase.



**Fig. 9.** Amplitude difference and phase difference of echo signals at the root end of a switch rail with/without defects: (a) amplitude difference and (b) phase difference.

### 3.1.3. Meshing method of defective parts of a switch rail

In order to reduce the impact of the meshing method of defects on the root-end echo, the defective area with the grid size of 2 mm to 5.5 mm was further refined. Then, the refined results were compared to those of the defect-free area. Three mesh refinement schemes were developed for the area on both sides of the defect: integral defect meshing scheme, progressive defect meshing scheme, and stepwise defect meshing

scheme.

The specific setting is shown in Fig. 10 and Table 3. The grid size of the whole switch rail was set to be 5.5 mm as an example. In Schemes 1 and 2, according to the integral defect meshing mode, the grid sizes in the defective Area A were respectively set to be 1 mm and 0.5 mm; the grid size in Area B on both sides of the defect was set to be 5.5 mm; the grid size in the remaining Area C was set to be 5.5 mm. In Schemes 3 and

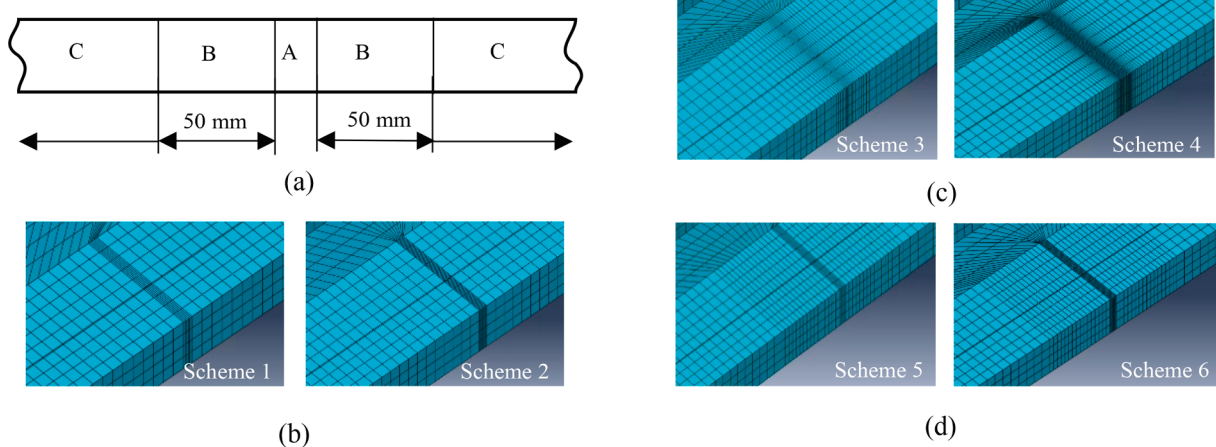


**Fig. 10.** Mesh refinement modes of the defective area: (a) regional map, (b) integral defect meshing mode, (c) progressive defect meshing mode, and (d) stepwise defect meshing mode.

**Table 3**

Mesh refinement schemes for switch rail defects.

Areas	Scheme 1	Scheme 2	Scheme 3	Scheme 4	Scheme 5	Scheme 6
A	1 mm	0.5 mm	1 mm	0.5 mm	1 mm	0.5 mm
B	5.5 mm	5.5 mm	5.5 mm-1 mm	5.5 mm-1 mm	2.7 mm	2.7 mm
C	5.5 mm	5.5 mm	5.5 mm	5.5 mm	5.5 mm	5.5 mm

4, according to the progressive meshing mode, the grid sizes in the defective Area A were respectively set to be 1 mm and 0.5 mm; the grid size in Area B on both sides of the defect gradually decreased from 5.5 mm to that in Area A; the grid size in the remaining Area C was set to be 5.5 mm. In Schemes 5 and 6, according to the progressive meshing mode, the grid sizes in the defective Area A was set to 1 mm and 0.5 mm; the grid size in Area B on both sides of the defect was set to be half of the grid size of the whole rail size, 2.7 mm; the grid size in the remaining Area C was set to 5.5 mm.

The three meshing modes of the defective area were further divided into six schemes. The amplitude difference and phase value difference of the signal at the root end of the switch rail after mesh refinement were compared with the results without refinement (Fig. 11). The amplitude difference and phase value difference in Schemes 3 and 4 were less than the unrefined results, indicating that the progressive defect meshing mode could lessen the amplitude difference and phase value difference caused by the presence of defects.

#### 3.1.4. Comparison of optimization results

The meshes of the defect at the rail bottom were refined with the progressive defect meshing mode (Fig. 12). The amplitude difference and phase value difference of the root end echoes of the switch rail with/without defects were the smallest and the consistent time-domain waveforms were observed. The effectiveness of the defect area refinement method was verified.

The amplitude difference and phase value difference in the simulation results without refining defect meshes were used to as original signals and the amplitude difference and phase value difference in the refined simulation results were used as calibration signals (Fig. 13). The amplitude difference and phase difference in calibration signals were

smaller than those in original signals under the excitation frequencies of 30 kHz, 70 kHz, and 100 kHz, indicating that the progressive meshing mode could increase the signal accuracy at the defect. The progressive meshing mode is applicable to a switch rail structure or a plate-type structure.

Based on the comprehensive consideration of calculation efficiency and accuracy, the grid sizes for excitation frequencies of 30 kHz, 70 kHz, and 100 kHz were set to be 5.5 mm, 4.5 mm, and 2.8 mm, respectively. The progressive meshing mode was adopted in the defective area and the above-mentioned parameters were used in subsequent FE modeling of the switch rail.

#### 3.2. Switch mechanism-switch rail contact mode setting

The switch mechanism is composed of bolts, connecting rods, connecting plates, and other mechanisms. In order to facilitate the repulsion and connection movement between switch mechanism and switch rail, connecting rods push (pull) connecting plates and two connecting plates are fixed onto the switch rail with bolts [49]. Fig. 14 is a schematic diagram of a switch rail. Under working conditions, fastening bolts are used to connect switch rail with switch mechanism. The multiple-scattering characteristics of guided waves at the connection complicate the signals detected by the sensor [50,51]. To accurately establish the 3D model of a switch rail and explore the propagation characteristics of guided waves in a switch rail, the influences of switch mechanism, root-end variable cross-section, and bolt hole on guided waves were investigated.

In this paper, 1:1 model of the switch rail was established with the FE method. Due to the complexity of the model, it is necessary to establish a two-dimensional model of different cross-sections. The lofting module was used to combine the two-dimensional models of multiple different cross-sections into a three-dimensional model (Fig. 14).

The interaction between switch mechanism and switch rail could be obtained by simulating the contact mode between connecting plates and switch rail. Two characteristic parameters of the materials of switch rail and connecting plates are shown in Table 4. The model mesh was chosen as hexahedral cell C3D8R for 3D meshing. The guided wave excitation position was 1.16 m away from the No. 1 switch mechanism at the rail bottom and the excitation signal was a Hanning window-

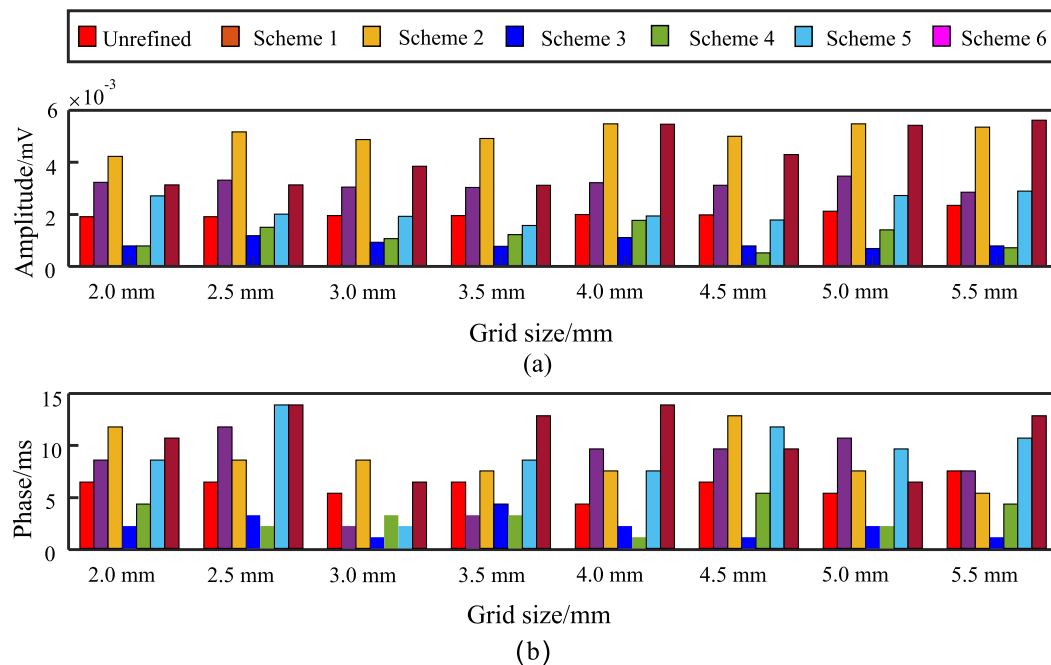
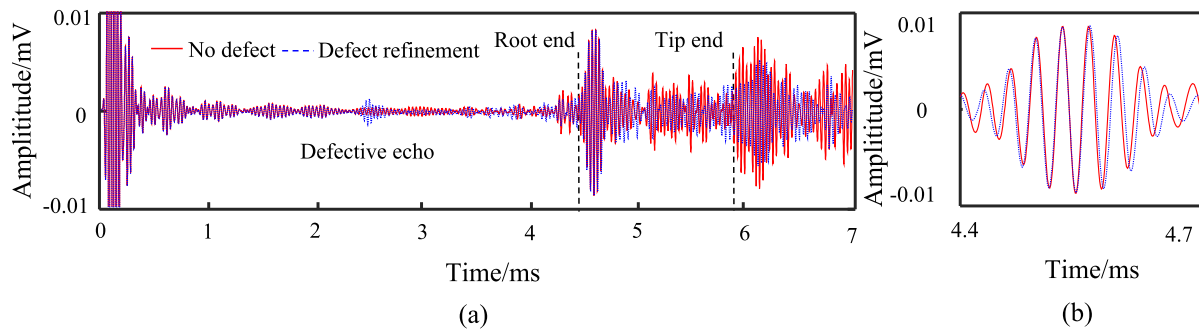


Fig. 11. Mesh refinement results of the defective area: (a) amplitude difference and (b) phase difference.



**Fig. 12.** Progressive meshing results of rail defects under the mesh size of 2 mm: (a) time-domain simulation results and (b) enlarged view of the root end of a switch rail.

modulated 5-cycle sine signal as follows:

$$x(t) = \left[ 0.5 \left( 1 - \cos \frac{2\pi f_c t}{n} \right) \sin(2\pi f_c t) \right] \quad (3)$$

where  $t$  is the time;  $n$  is the number of periods;  $f_c$  is the central frequency of the signal.

According to actual working conditions, FE setting methods of switch mechanism can be divided into three categories: tie constraint, normal constraint, and tangential constraint. The effects of tie constraint, normal constraint, and tangential constraint on the guided waves were studied and the correlation between simulation results and experimental signals was analyzed to determine relative errors.

### 3.2.1. Tie constraint

Tie constraint is to bind the two regions of the model together so that the relative movement between the two parts does not occur. Fig. 15(a)-15(b) show the sensor layout with/without the rutting mechanism at 30 kHz and Fig. 15(c) shows the time domain simulation results of the guided wave when the Tie constraint is applied to the switch structure.

The No. 1 switch mechanism was 1.16 m away from the sensor and the defect was 2.5 m away from the sensor. With the group velocity of 3260 m/s in the steel plate, the propagation period of reflected echo was estimated. The reflected echo propagated in the No. 1 switch mechanism in the period from 0.7 ms to 1.0 ms, and the reflected echo propagated in the defect in the period from 1.5 ms to 1.8 ms. The period from 0 ms to 1.8 ms was selected as the observation interval of the switch machine simulation. Fig. 15(d)-15(f) show the time domain simulation results of the guided wave with/without the rutting mechanism of the pointed rail at excitation frequencies of 30 kHz, 70 kHz and 100 kHz as well as experimental results. Simulation 1 indicates the simulation result obtained without switch mechanism. Simulation 2 indicates the simulation result obtained with switch mechanism. The comparison between simulated signals and experimental signals indicated that the reflected echoes of the switch mechanism appeared in the period from 0 ms to 1.8 ms.

The main cause of the amplitude inconsistency between the experimental signal and simulation signal in Fig. 15(d-f) is the detection of the instrument excitation signal. The instrument is used as an integrated device and has a fixed excitation amplitude and amplification, which causes a larger amplitude of the signal in the experiment. For the analysis of the data, the main information extracted is the time information in the echo signal, so the amplitude deviation will not have an effect on the detection of the signal.

To quantify the similarity between simulation and experimental results, the reflected echo signals of the switch mechanism in the simulation results are intercepted with the Hilbert envelope method to analyze their correlation with experimental echo signals (Fig. 16). Under this constraint, the simulation results of the switch mechanism were positively correlated with the experimental results at different

frequencies of guided waves. The correlation coefficients were higher than 0.6, indicating that the strong correlation between simulation and experimental results.

The peak amplitudes and RMS (Root Mean Square) values of echo signals from the original defect and the switch mechanism in the simulation and experimental results were compared and the relative errors between simulation and experimental results were calculated (Table 5). Under tie constraint, the relative error of the amplitude ratio between simulated signals and experimental signals at different frequencies was less than 10% and the relative error of RMS ratio between simulated signals and experimental signals was less than 12%.

### 3.2.2. Normal constraint

Normal constraint is another setting method used in the switch machine structure simulation model. The rated traction force designed for the switch mechanism is 5.9 kN/9Mpa. When the overall pressure is 12 Mpa, the corresponding traction force is 7.9 kN. To explore the propagation characteristics of the guided wave in the switch rail when connecting plates were subjected to various normal constraints, the normal constraint was set to be 0 to 10 kN with an interval of 2 kN. Fig. 17 illustrates the simulation results under different normal constraints. At 30 kHz, the amplitude of the reflected echo from the switch mechanism steadily rose as the normal constraint increased because the reflected guided wave was gradually enhanced when the normal constraint increased and the contact between the connecting plate and switch rail became closer.

The peak amplitude ratio and RMS value ratio between the reflected echoes signa of the switch mechanism and the reflected echo signal of the original defect in the simulation results at various frequencies were calculated, and compared with those of experimental signals to calculate the relative errors (Fig. 18). As the normal constraint increased, the amplitude ratios and RMS ratios between simulated signals steadily increased, whereas the relative error firstly decreased and then increased. When the mean normal constraint was 6 kN, the relative errors between experimental signals and simulated signals were the smallest, demonstrating that the normal constraint applied to connecting plates could imitate the actual operation conditions of the switch mechanism.

### 3.2.3. Tangential constraint

In tangential constraint, the contact status between connecting plates and the rail was changed by setting the value of the penalty function. The connecting plate was set as the master surface and the contact position between the rail and connecting plates was set as the slave surface. The range of penalty function was set to be 0.0 to 1.0 and the interval was 0.2. Under the above settings, the effects of the switch mechanism on the reflection echoes of guided waves with different tangential constraints were explored. The amplitude of the reflected echoes from the switch mechanism gradually increased as the tangential constraint

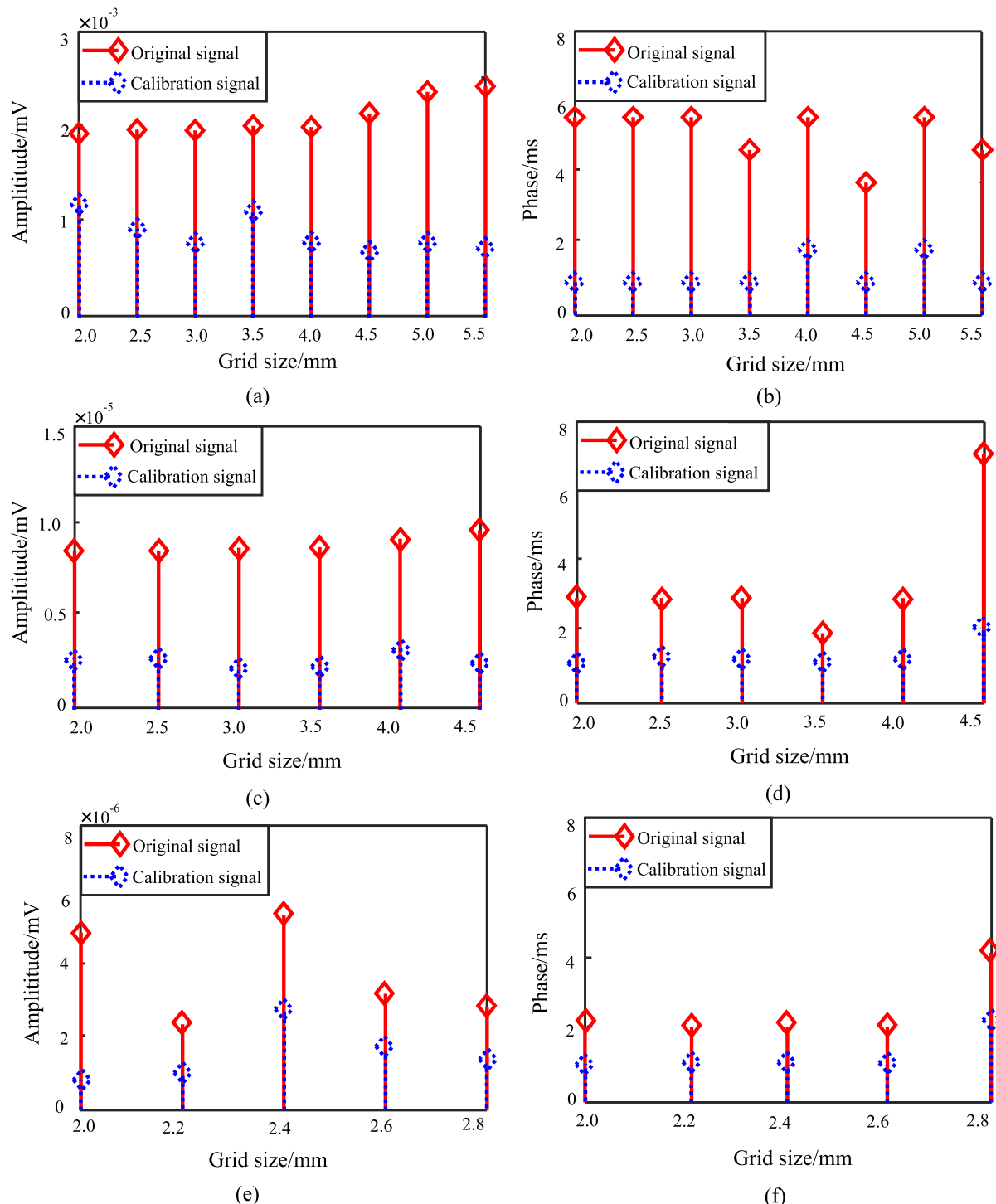


**Fig. 13.** Comparative analysis of original signals and the calibration signals: (a) amplitude difference at 30 kHz, (b) phase difference at 30 kHz, (c) amplitude difference at 70 kHz, (d) phase difference at 70 kHz, (e) amplitude difference at 100 kHz, and (f) phase difference at 100 kHz.

increased (Fig. 19).

The amplitude ratio and RMS values ratio between the switch mechanism echo signal and the original defect reflection echo signal in the simulation results at different frequencies were calculated, and compared with those of experimental signals (Fig. 20). The correlation coefficient between the simulated and experimental signals at the same frequency did not vary with the tangential constraint. As tangential constraint increased, the amplitude ratio and RMS ratio between simulated signals gradually increased, but the relative error firstly decreased

and then increased. The effects of different frequencies on the tangential constraint differed because low-frequency guided waves propagated mainly at rail bottom; medium-frequency guided waves mainly propagated at rail web; high-frequency guided waves mainly propagated at rail head [52]. The rail web was the main stress bearing location from tangential restraint, so the amplitude ratio at 70 kHz was less than that at 30 kHz and 100 kHz.

In summary, under the excitation frequency of 70 kHz, when the tangential constraint was 0.4, the relative errors between simulated and

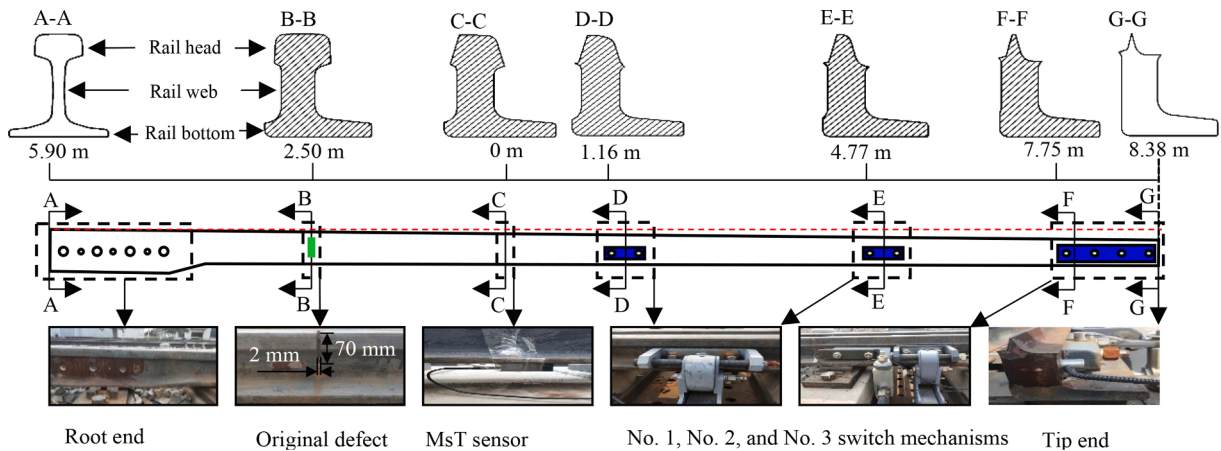


Fig. 14. Partial sectional view of a switch rail.

**Table 4**  
Setting of material parameters.

Parameters	Density ( $\text{kg}/\text{m}^3$ )	Elastic modulus (GPa)	Poisson ratio
Switch rail	7890	210	0.3
Connecting plate	7890	210	0.3

experimental signals were the smallest. Under excitation frequencies of 30 kHz and 100 kHz, when the tangential constraint was 0.6, the relative errors between simulated and experimental signals were the smallest.

### 3.2.4. Comparison of three constraints

The setting method with the smallest relative error was selected as the basis for the subsequent study. The relative error of tie constraint was lower than the relative errors of normal and tangential constraints at excitation frequencies of 70 kHz and 100 kHz (Fig. 21), indicating that tie constraint could improve simulation accuracy and make the model closer to the actual operation conditions of a switch rail. Therefore, tie constraint is adopted in the FE setting of the switch mechanism.

### 3.3. Variable cross-section at the root end of a switch rail

#### 3.3.1. Model establishment

The root end of the switch rail was set to be the same as the rail section (Sections A-A and B-B in Fig. 14). Behind the variable cross-section, the dimensions of rail head, rail web, and rail bottom of the switch rail were reduced. The transition area and the rail area were respectively set as Areas I and II. In Area II of rail web, there were 3 bolt holes with a radius of 20 mm and 2 stress relief holes with a radius of 2.5 mm. The switch rail was connected to the rail by means of bolt holes and connecting plate. Fig. 22 shows the main and top views of the variable cross-section of the root end.

In existing mesh generation methods, seeds are firstly arranged for the geometric model to control the unit density and position and then meshes are directly generated with the automatic algorithm. This division is not applicable in switch rail. The root end of the switch rail is a complex structure, so direct cell assignment and meshing will lead to a warning of mesh transition distortion, as shown in the highlighted area in Fig. 23(a) [53]. The redundant part of the variable cross-section at the root end of the switch rail was removed by partitioning cells and the root end of the switch rail was divided into several zones (Fig. 23). After splitting geometric constraints, the switch rail was meshed with hexahedral cells.

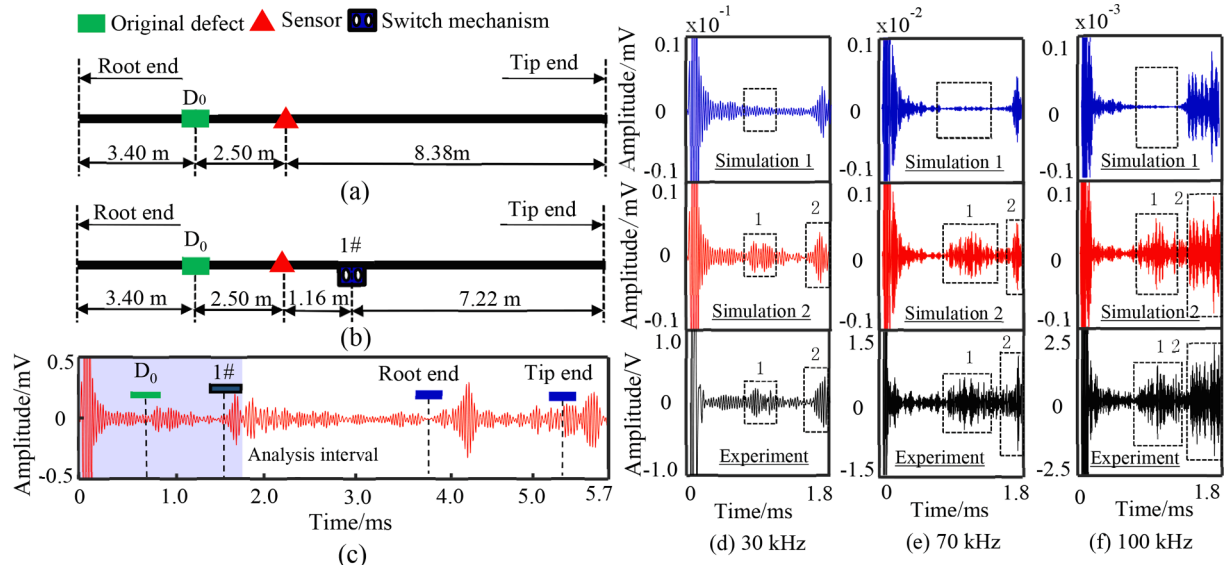
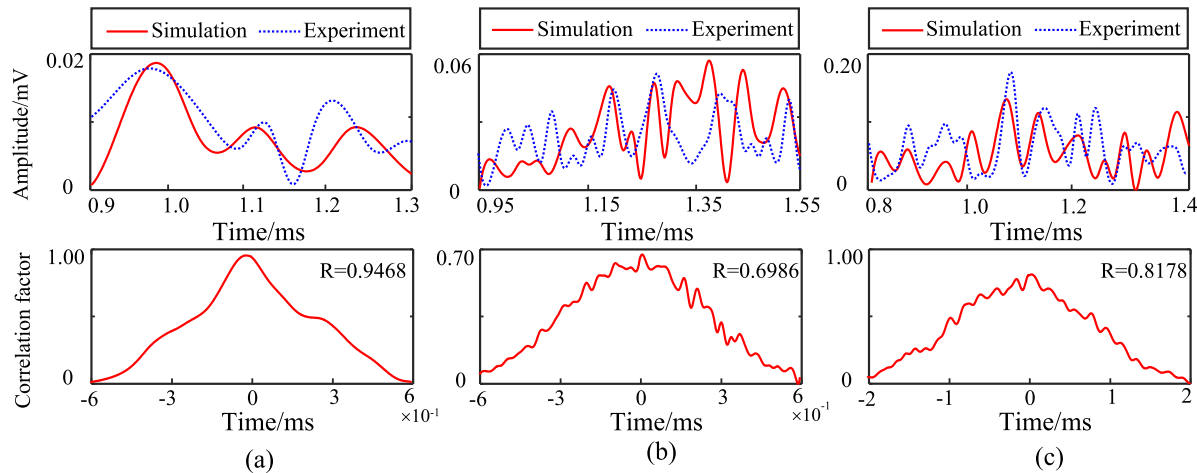


Fig. 15. Time-domain signal diagram of switch mechanism: (a) sensor layout diagram without switch mechanism, (b) sensor layout diagram of switch mechanism, (c) time domain signal diagram, (d) 30 kHz, (e) 70 kHz, and (f) 100 kHz.



**Fig. 16.** Cross-correlation calculation results of tie constraint simulation of the switch mechanism at different excitation frequencies: (a) 30 kHz, (b) 70 kHz, and (c) 100 kHz.

**Table 5**

Cross-correlation analysis of tie constraint simulation results and experimental signals at different frequencies.

Stimulation frequencies	Amplitude ratio			RMS ratio		
	Simulation	Experiment	Relative error		Simulation	Experiment
30 kHz	0.6143	0.5674	8.27%	0.5902	0.6409	7.91%
70 kHz	0.5995	0.5590	7.26%	0.5907	0.5572	6.02%
100 kHz	0.7204	0.6808	5.82%	0.5798	0.5185	11.82%

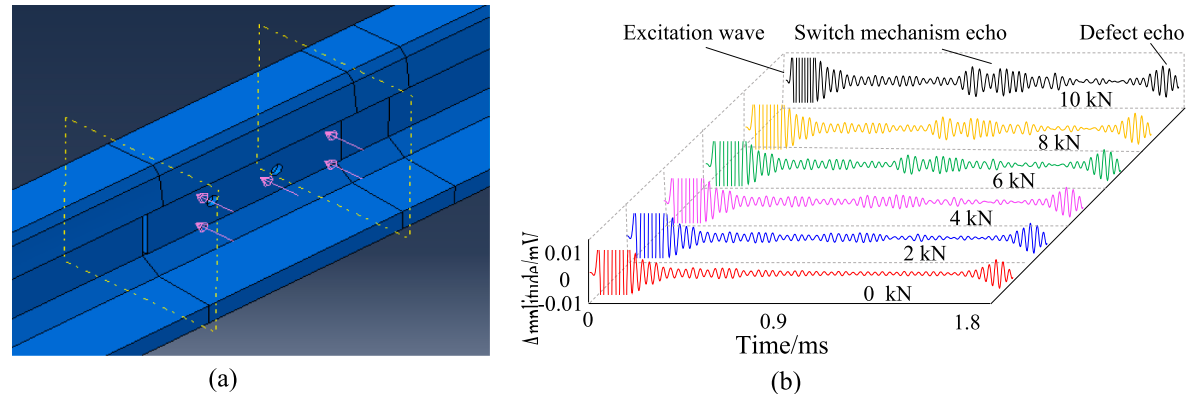


**Fig. 17.** Normal constraint FE setting method and simulation results: (a) simulation setting and (b) time-domain simulation results under different normal constraints.

### 3.3.2. Model validation

The simulation results of the echoes from the root-end of the switch rail under the frequency of 30 kHz are shown in Fig. 24. Simulated results of the echoes from the switch rail without variable cross-section are shown in Simulation 1. Simulated results of the echoes from the switch rail with variable section are shown in Simulation 2. Simulated results of the echoes from the switch rail with variable cross-section containing bolt holes are shown in Simulation 3. From Simulation 1 to Simulation 3, the simulation results were closer to the root end of switch rail. Both the simulated and experimental signals showed the reflected echoes of characteristic structures, such as the echoes from switch mechanism, original defect echoes, and root end. The root end of the switch rail was complicated due to the presence of variable cross-section, bolt holes, and other characteristic structures, so echo signals from the root end were more complex. With the gradual change of the root end, the echo signals from the root end in the simulation were similar to the experimental echo signals, thus proving the correctness of the FE model.

In order to further prove whether the finite element model can be used to simulate the actual switch rail, the peak-to-peak values and RMS values of the reflected echo signals of the root-end variable section in the simulation and experiments are extracted and analyzed by the correlation analysis and relative error analysis and the calculation results are shown in Tables 6 and 7. According to the calculation results, the correlation coefficient value increases gradually from the root end of the switch rail without variable section to the root end of the switch rail with variable section and finally to the variable section plus hole model. This finding shows that the model and the variable section part of the actual switch rail are becoming more similar over time. The similarity between the model and the real switch rail can be explained by the relative error between the experimental signal and the simulated signal, which showed that the relative error gradually decreased from the root end of the switch rail without variable section to the model with variable section and hole.

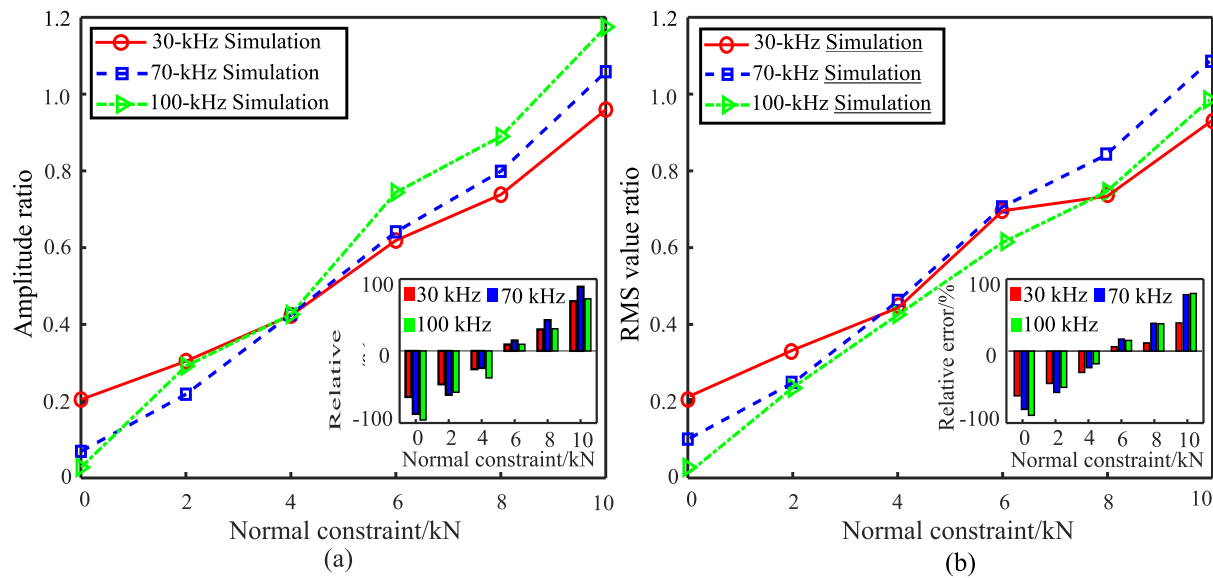


**Fig. 18.** Amplitude ratio and RMS value ratio of different load forces and experimental signals at different frequencies: (a) amplitude ratio, (b) RMS value ratio.

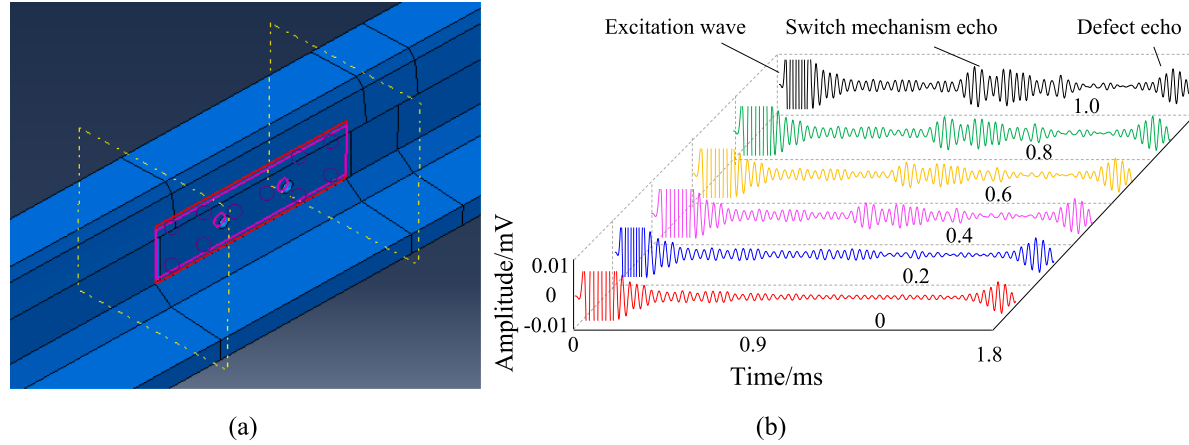


**Fig. 19.** Interaction FE setting method and simulation results: (a) simulation setting and (b) time-domain simulation results under different tangential constraints.

### 3.3.3. Bolt hole analysis

In order to further investigate the effects of bolt holes at the root end of the switch rail on the guided waves at different frequencies. The time domain simulation signal of variable section and the time domain signal of variable section with bolt hole were analyzed according to the difference method. Fig. 25(a) depicts the differences of two signals on the guided wave at excitation frequencies of 30 kHz, 70 kHz, and 100 kHz.

The energy values of the reflected echoes from bolt holes are calculated (Fig. 25(b)). The energy value of the reflected wave from bolt holes was also calculated. As the frequency increased, the reflected echoes from bolt holes increased and the energy of the reflected echoes gradually decreased. The low-frequency guided wave showed the stronger reflection at bolt holes than the high-frequency guided wave and the excited mode was mainly SH0-like mode. The reflected echo from bolt holes was also mainly in SH0-like mode and the energy loss caused by reflection was less.

The  $n$ -order cutoff frequency of the SH guide wave is given by:

$$(fd)_n = \frac{nc_T}{2} \quad (4)$$

where  $f$  is the cut-off frequency;  $d$  is the thickness of the waveguide structure;  $c_T$  is the phase velocity of the guided wave.

Generally, the cutoff frequency of SH1-like guided wave in a 25-mm

thick board is 67 kHz. SH1-like mode guide waves were generated when the excitation frequencies were 70 kHz and 100 kHz. Therefore, high-frequency waves and more energy was lost during mode transition, and low-frequency guided waves were suitable for detecting bolt holes.

## 4. Analysis of experimental results

### 4.1. Time-domain analysis method

The propagation characteristics of guided waves with different frequencies in the absence of rail defects, rail head defect and rail bottom defect were studied with the calibrated model, and compared with experimental results. The experimental signal of a switch rail without defect, a switch rail with a head defect, and a switch rail with a bottom defect were compared with the simulation signal at the excitation frequency of 30 kHz (Fig. 26) so as to analyze the time-domain results. Simulation 1 and Experiment 1 show the signal of a switch rail without defect. Simulation 2 and Experiment 2 show the signal of a switch rail with a head defect. Simulation 3 and Experiment 3 indicate the signal obtained after adding the rail bottom defect to the rail head defect.

The results of Simulation 1, Experiment 1, Simulation 2, Experiment 2, Simulation 3, and Experiment 3 were compared. The reflected echoes of characteristic structures were observed in the same time interval. In

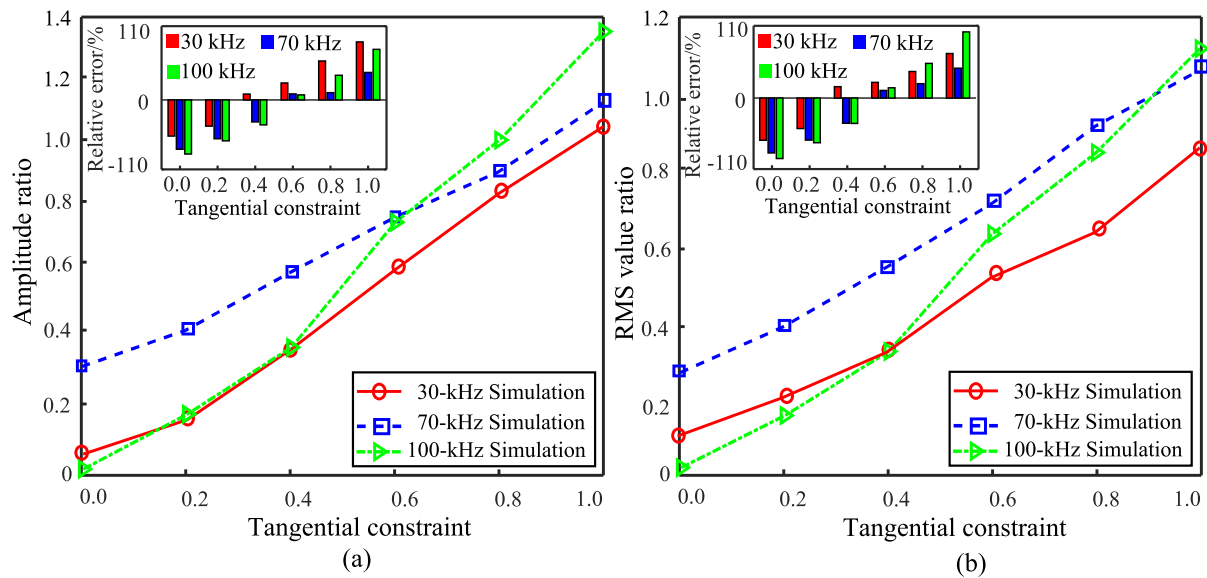


**Fig. 20.** Amplitude ratio and RMS value ratio of different friction coefficients and experimental signals at different frequencies: (a) amplitude ratio, and (b) RMS value ratio.

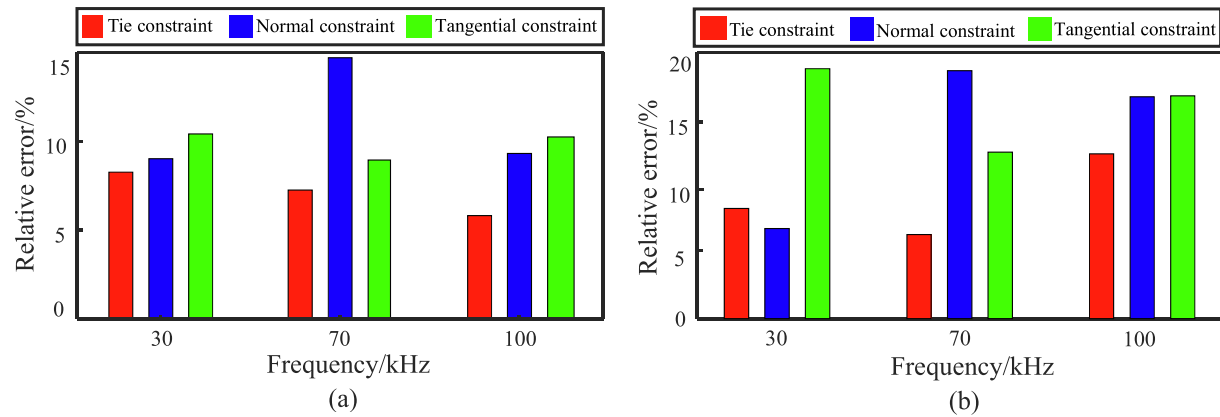


**Fig. 21.** Comparison of the relative errors between simulation results of three setting methods and experimental signals: (a) relative error of amplitude ratio and (b) relative error of RMS ratio.

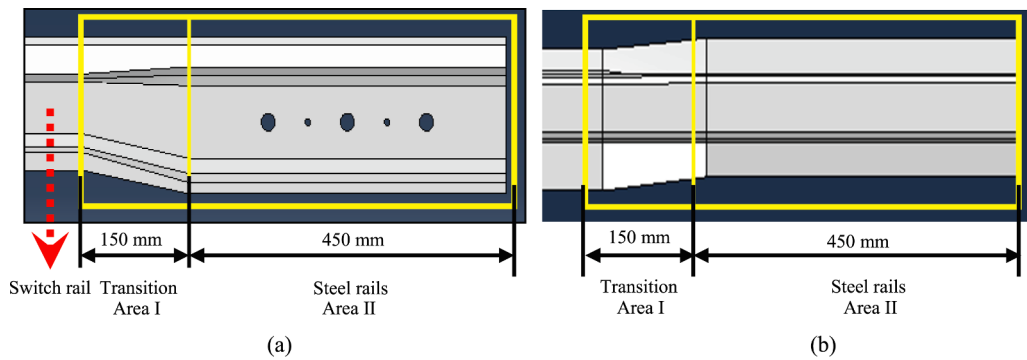


**Fig. 22.** Schematic diagram of the variable cross-section at the root end of switch rail: (a) main view and (b) top view.

the interval from 0.7 to 1.8 ms, the reflected echo signal of No. 1 switch mechanism structure was observed in both simulation and experimental results. In the interval from 3.8 to 4.5 ms, the reflected echo signal of the root end of the switch rail appeared. After adding rail head and rail bottom defects, the obtained signals were compared with those obtained

without defect and the defect echo signal could be observed. Due to the existence of defects, the guided wave energy was reflected and transmitted and the amplitude of the reflected echo of the defective rear end of the characteristic structures such as the switch rail tip was reduced. In the experimental and simulation results, the amplitude of the reflected

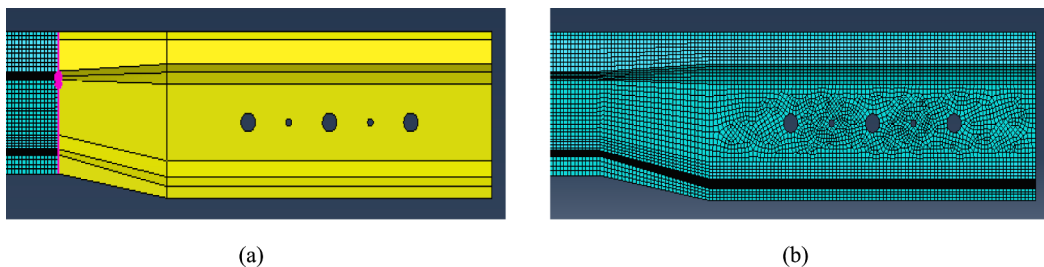


**Fig. 23.** Mesh division of variable cross-section at the root of the switch rail: (a) undivided geometric elements and (b) divided geometric elements.

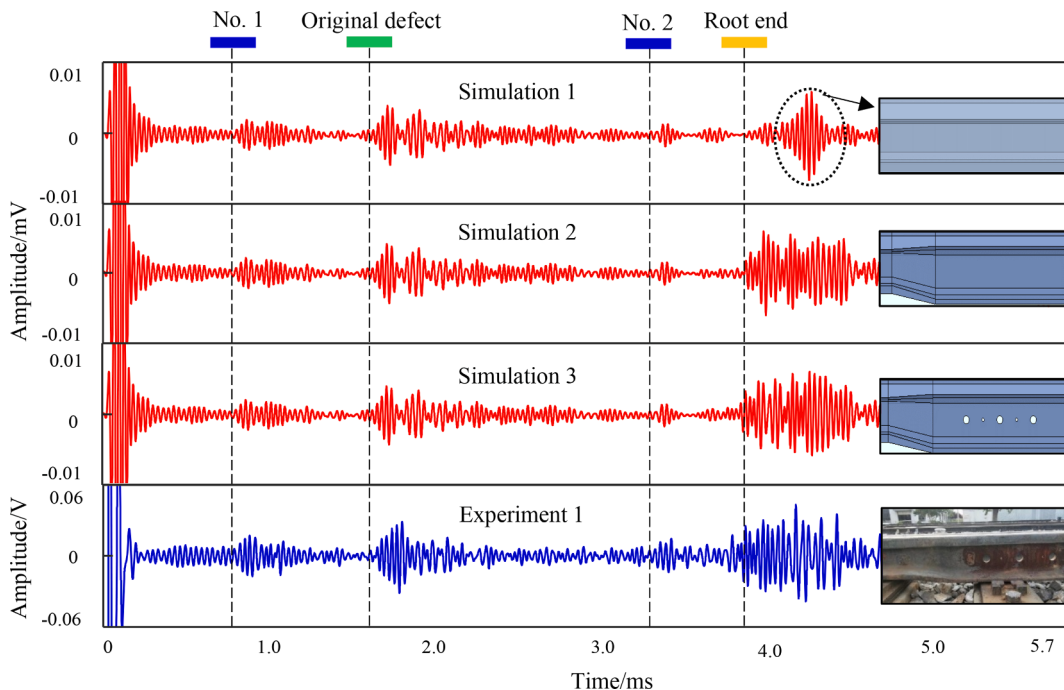


**Fig. 24.** Simulation results of the echoes from the root end of switch rail under the excitation frequency of 30 kHz.

**Table 6**

Calculation results, experimental results, and relative errors of amplitude from the variable cross-section root end of the switch rail under the excitation frequency of 30 kHz.

Root end types	Correlation factor	Amplitude		
		Simulation	Experiment	Relative error
No variable section	0.1420	0.0684	0.0828	17.39%
Variable section	0.3601	0.0708	0.0828	14.49%
Variable section with holes	0.3989	0.0072	0.0828	13.04%

**Table 7**

Calculation results, experimental results, and relative errors of RMS value from the variable cross-section root end of the switch rail under the excitation frequency of 30 kHz.

Root end type	Correlation coefficients	RMS values		
		Simulation	Experiment	Relative error
No variable section	0.1420	0.0108	0.0173	37.57%
Variable section	0.3601	0.0156	0.0173	9.83%
Variable section with holes	0.3989	0.0168	0.0173	2.89%

echo firstly increased and then decreased. The comparison of various parameters between simulation and experimental results showed that the developed FE model of the switch rail could be used to predict various problems of switch rails.

The group velocity of the SH0 guided wave in steel plate (3260 m/s) was adopted in this study. As indicated by the calculated results, the rail head defect was between 2.6 ms and 3.4 ms and the rail bottom defect was between 4.2 ms and 4.9 ms. The calculation results were consistent with the actual situation.

#### 4.2. Time-frequency analysis

With the difference method, the guided wave changes caused by the rail head defect could be determined from the simulation echoes of the rail with head defect and the simulation echoes of the rail without head defect. Similarly, the guided wave changes caused by the rail bottom defect could be determined. The simulation and experimental reflected echoes from rail head defect and rail bottom defect at various frequencies are respectively depicted in Figs. 27(b) and 28(b).

At an excitation frequency of 30 kHz, the reflected echo from the rail bottom defect had the larger amplitude compared with that from the rail head defect. At an excitation frequency of 70 kHz, the reflected echo from the rail bottom defect had the same amplitude compared with that from the rail head defect. At an excitation frequency of 100 kHz, the reflected echo from the rail bottom defect had the lower amplitude

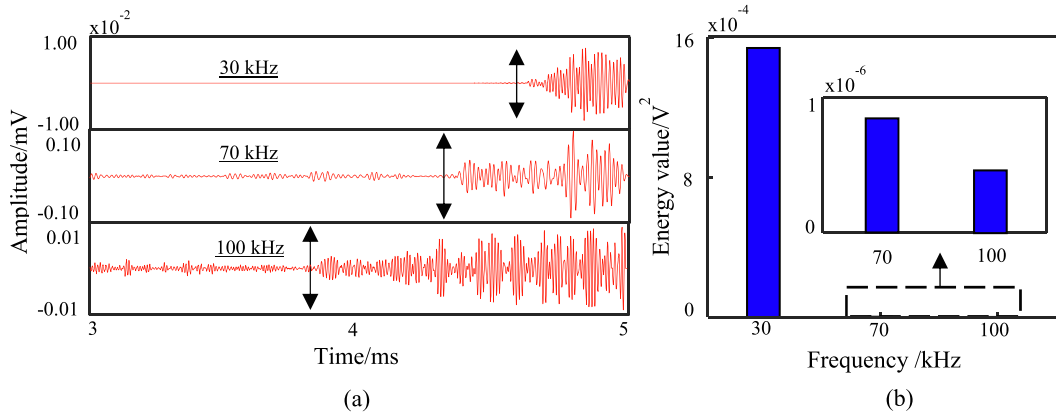


**Fig. 25.** Interaction between guided waves at different frequencies and bolt holes: (a) time-domain diagram and (b) energy value.

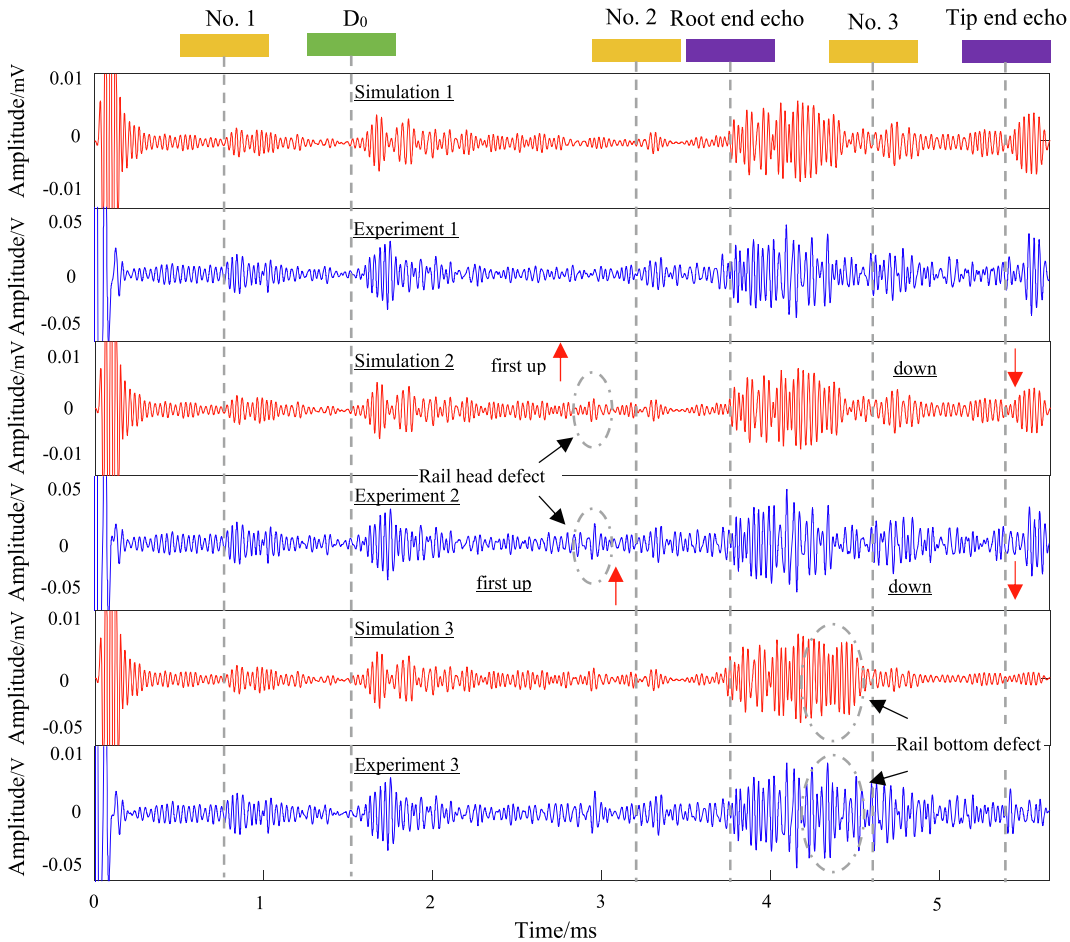


**Fig. 26.** Comparison of simulated and experimental time-domain signals under the excitation frequency of 30 kHz.

compared with that from the rail head defect.

Short-Time Fourier Transform (STFT) was used to explore the signal in two aspects: time and frequency [54]. The simulated and experimental time-frequency diagrams of the rail head defect are respectively shown in Figs. 27(a) and 28(a). The simulated and experimental time-frequency diagrams of the rail bottom defect are respectively shown in Figs. 27(c) and 28(c). In the longitudinal analysis, with the increase in the frequency, the echo signals from rail head defect and rail bottom defect became more complicated. The cross-sectional analysis results revealed that guided waves at 30 kHz and 100 kHz were respectively sensitive to rail bottom defects and rail head defects, whereas guided

waves at 70 kHz were sensitive to both rail bottom defects and rail head defects.

Each pixel reflects the average power of the signal in the time domain per unit frequency band, namely, power spectral density (PSD), so that the distribution of the average power of the signal in the frequency domain can be obtained (Figs. 27(a), 27(c), 28(a) and 28(c)) [55,56]. The average power values of the defect echo signals at different frequencies are shown as the blue dashed line in Fig. 29. The PSD values of reflected echoes from rail head defects were much lower than rail bottom defects when low-frequency (30 kHz) guided waves propagated in switch rails. The PSD of the reflected echo of a rail head defect was

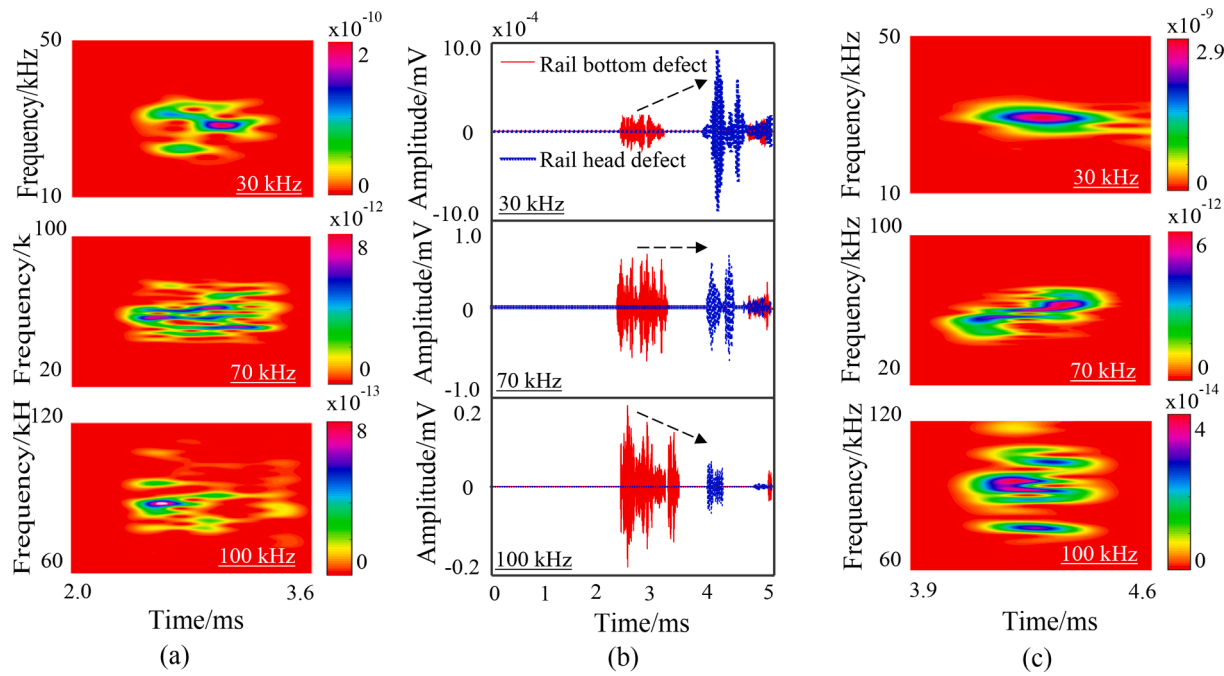


**Fig. 27.** Simulation results of guided waves with different frequencies and reflected echoes from rail head and rail bottom defects: (a) rail head defect STFT transformation, (b) defect time-domain signals, and (c) rail bottom defect STFT transformation.

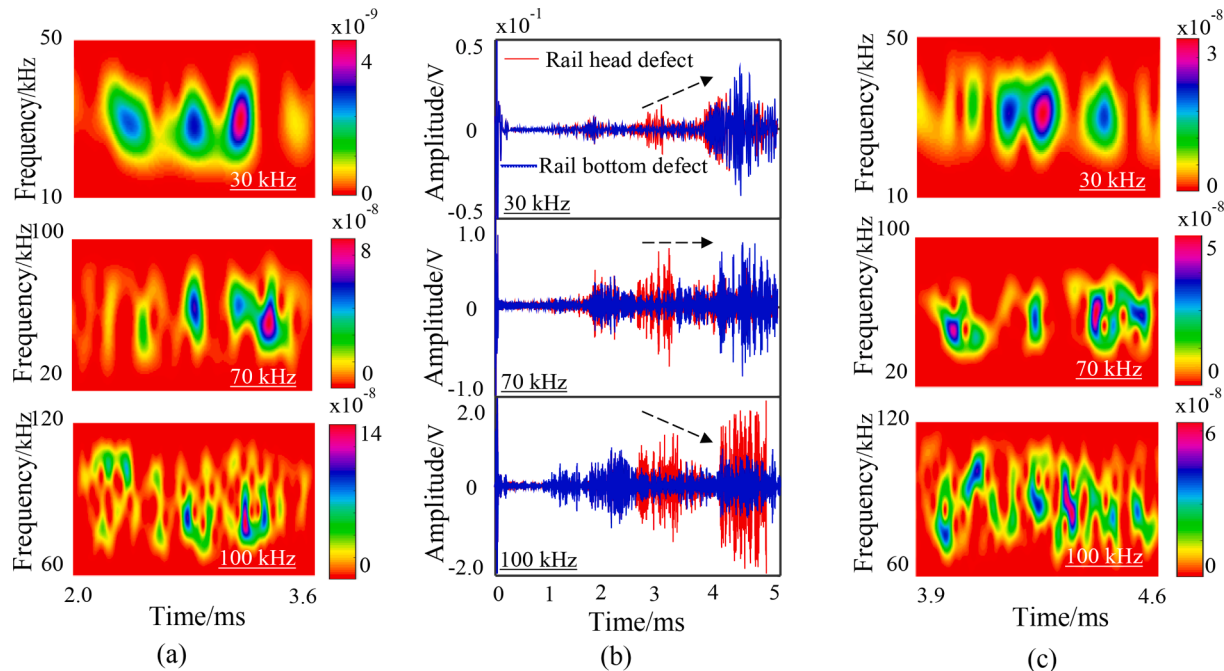


**Fig. 28.** Experimental results of guided waves with different frequencies and reflected echoes from rail head and rail bottom defects: (a) rail head defect STFT transformation, (b) defect time-domain signals, and (c) rail bottom defect STFT transformation.

second to that rail bottom defect when the medium frequency (70 kHz) guided wave propagated in a switch rail. When high-frequency (100 kHz) guided waves propagated in a switch rail, the PSD values of the reflected echoes from the rail head defect were much higher than rail bottom defect, indicating that high-frequency guided waves were sensitive to rail head defects and applicable to detect rail head defects. Low-frequency guided waves were sensitive to rail bottom defects and applicable to detect rail bottom defects.

## 5. Conclusion

In this study, a FE model of a switch rail was established to accurately predict the defect information in the switch rail and provided the basis for the health monitoring of switch rails. In the establishment of the simulation model, mesh size at various frequencies, mesh optimization of the defective areas, contact setting between switch mechanism and switch rail, and meshing methods at the root of the switch rail were investigated. Firstly, the validity of the model was demonstrated

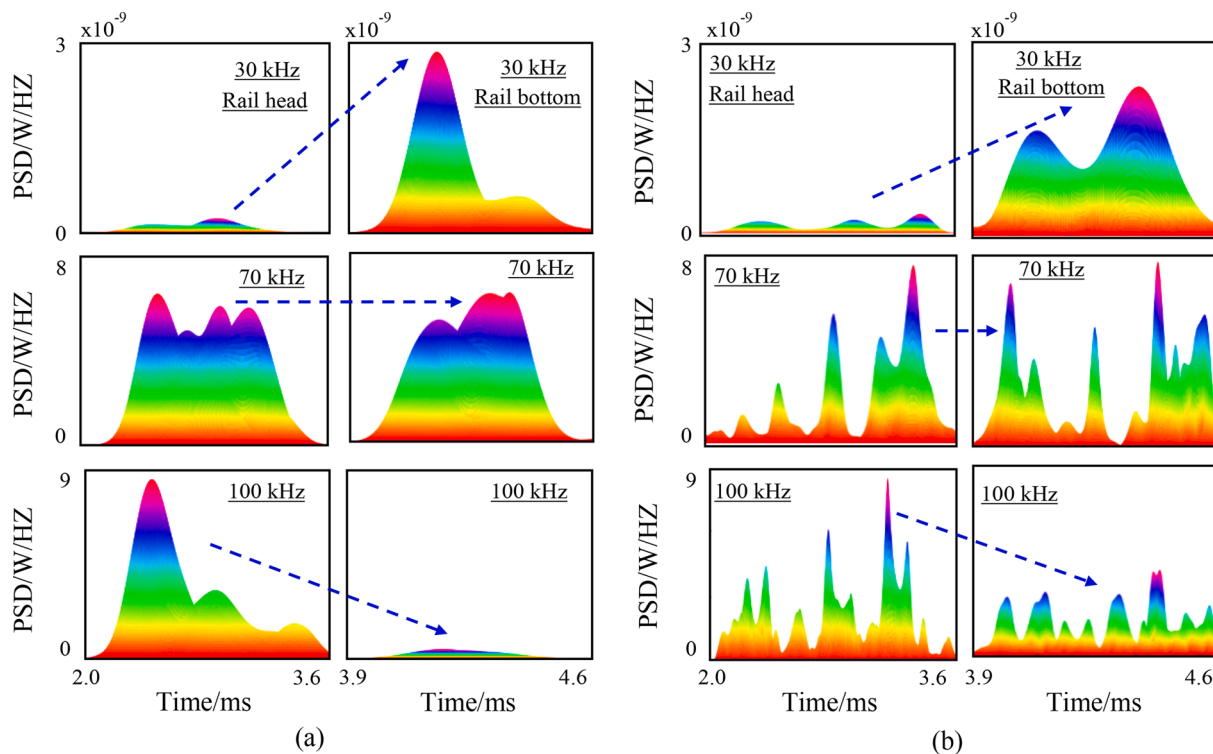


**Fig. 29.** PSD distributions of guided waves at different frequencies for defects at different positions: (a) defect detection simulation results and (b) defect detection experimental results.

experimentally. The model was then used to explore the interaction between guided waves of different frequencies and defects in the rail head and rail bottom of the switch rail.

The main conclusions are drawn as follows:

- The optimal grid size of the switch rail was set to be 5.5 mm under an excitation frequency of 30 kHz; the grid size was set to be 4.5 mm under an excitation frequency of 70 kHz excitation frequency; the grid size was set to be 2.8 mm under an excitation frequency of 100 kHz. The defect area was divided with a progressive meshing mode.
- In the switch mechanism simulation, compared to normal constraint and tangential constraint, the tie constraint setting method could increase simulation accuracy and decrease the relative error between the model and the actual switch rail.
- FE models could simulate the propagation characteristics of guided waves in actual switch rails and predict information about defects in switch rails. Guide waves with different frequencies interacted with defects differently. Low-frequency SH-like guide waves were applicable to detect rail bottom defects, whereas high-frequency SH-like guide waves were applicable to detect rail head defects.

The sensor reliability should be confirmed through long-term monitoring. The circuit of the guided wave detection instrument is relatively large and the circuit has not yet been miniaturized. The battery power supply will be changed into solar power supply in the future. In this paper, only the detection of rail head and rail bottom defects is considered. The subsequent research will further consider the detection of rail web defects and realize the integrity detection of the whole section of the rail. In the future, the finite element model calibrated by experimental results can be used to simulate the guided wave detection of any defect at any position. It is significant in signal recognition for optimizing the switch rail guided wave detection scheme.

#### CRediT authorship contribution statement

**Xiafei Li:** Data curation, Methodology, Writing – original draft, Writing – review & editing. **Bin Wu:** Funding acquisition, Project administration, Resources. **Xiang Gao:** Formal analysis, Methodology, Writing – original draft, Writing – review & editing. **Yao Liu:** Validation, Visualization. **Huan Wang:** Data curation. **Xiucheng Liu:** Data curation, Methodology, Resources.

#### Declaration of Competing Interest

The authors declare that they have no known competing financial interests or personal relationships that could have appeared to influence the work reported in this paper.

#### Data availability

Data will be made available on request.

#### Acknowledgments

This work is supported by National Natural Science Foundation of China Grant numbers: 12272014, 12004018, 12122201.

#### Appendix A. Supplementary data

Supplementary data to this article can be found online at <https://doi.org/10.1016/j.measurement.2023.113325>.

#### References

- [1] W. Chen, W. Liu, K. Li, P. Wang, H. Zhu, Y. Zhang, C. Hang, Rail crack recognition based on Adaptive Weighting Multi-classifier Fusion Decision, Measurement: J. Int. Meas. Confederation 123 (2018) 102–114, <https://doi.org/10.1016/j.measurement.2018.03.059>.

- [2] H. Ge, D. Chua Kim Huat, C.G. Koh, G. Dai, Y. Yu, Guided wave-based rail flaw detection technologies: state-of-the-art review, *Struct. Health Monit.* 21 (3) (2022) 1287–1308.
- [3] S. Coccia, I. Bartoli, A. Marzani, F. Lanza Di Scalea, S. Salamone, M. Fateh, Numerical and experimental study of guided waves for detection of defects in the rail head, *NDT and E Int.* 44 (2011) 93–100, <https://doi.org/10.1016/j.ndteint.2010.09.011>.
- [4] G. Jing, M. Siahkouhi, K. Qian, S. Wang, Development of a field condition monitoring system in high speed railway turnout, *Measurement* 169 (2021) 108358.
- [5] X. Cao, W. Xie, S.M. Ahmed, C.R. Li, Defect detection method for rail surface based on line-structured light, *Measurement* 159 (2020) 107771.
- [6] W. Liu, Z. Tang, F. Lv, X. Chen, Multi-feature integration and machine learning for guided wave structural health monitoring: Application to switch rail foot, *Struct. Health Monit.* 20 (2021) 2013–2034, <https://doi.org/10.1177/147592172198577>.
- [7] P. Cawley, Structural health monitoring: Closing the gap between research and industrial deployment, *Struct. Health Monit.* 17 (2018) 1225–1244, <https://doi.org/10.1177/1475921717750047>.
- [8] W.F. Zhu, Y.X. Xiang, H.Y. Zhang, Y. Cheng, G.P. Fan, H. Zhang, Research on ultrasonic sparse DC-TFM imaging method of rail defects, *Measurement (Lond.)* 200 (2022), <https://doi.org/10.1016/j.measurement.2022.111690>.
- [9] S. Rodriguez, V. Gayoux, E. Ducasse, M. Castaings, N. Patteeuw, Ultrasonic imaging of buried defects in rails, *NDT and E Int.* 133 (2023) 102737.
- [10] P. Rizzo, F.L. di Scalea, Feature extraction for defect detection in strands by guided ultrasonic waves, *Struct. Health Monit.* 5 (2006) 297–308, <https://doi.org/10.1177/1475921706067742>.
- [11] M. Zhao, W. Zhou, Y. Huang, H. Li, Sparse Bayesian learning approach for propagation distance recognition and damage localization in plate-like structures using guided waves, *Struct. Health Monit.* 20 (2021) 3–24, <https://doi.org/10.1177/1475921720902277>.
- [12] P. Rizzo, M. Cammarata, I. Bartoli, F.L. di Scalea, S. Salamone, S. Coccia, R. Phillips, Ultrasonic guided waves-based monitoring of rail head: Laboratory and field tests, *Adv. Civil Eng.* 2010 (2010) 1–13.
- [13] P.W. Loveday, C.S. Long, D.A. Ramatlo, Ultrasonic guided wave monitoring of an operational rail track, *Struct. Health Monit.* 19 (2020) 1666–1684, <https://doi.org/10.1177/1475921719893887>.
- [14] H. Ge, D. Chua Kim Huat, C.G. Koh, G. Dai, Y. Yu, Guided wave-based rail flaw detection technologies: state-of-the-art review, *Struct. Health Monit.* 21 (3) (2022) 1287–1308.
- [15] D.A. Ramatlo, D.N. Wilke, P.W. Loveday, Development of an optimal piezoelectric transducer to excite guided waves in a rail web, *NDT and E Int.* 95 (2018) 72–81, <https://doi.org/10.1016/j.ndteint.2018.02.002>.
- [16] M. Pathak, S. Alahakoon, M. Spiriyagin, C. Cole, Rail foot flaw detection based on a laser induced ultrasonic guided wave method, *Measurement* 148 (2019) 106922.
- [17] J. Zhang, H. Ma, W. Yan, Z. Li, Defect detection and location in switch rails by acoustic emission and Lamb wave analysis: A feasibility study, *Appl. Acoust.* 105 (2016) 67–74, <https://doi.org/10.1016/j.apacoust.2015.11.018>.
- [18] D.A. Ramatlo, D.N. Wilke, P.W. Loveday, Development of an optimal piezoelectric transducer to excite guided waves in a rail web, *NDT and E Int.* 95 (2018) 72–81, <https://doi.org/10.1016/j.ndteint.2018.02.002>.
- [19] J. Wu, Z. Tang, F. Lü, K. Yang, Ultrasonic guided wave focusing in waveguides with constant irregular cross-sections, *Ultrasonics* 89 (2018) 1–12, <https://doi.org/10.1016/j.ultras.2018.04.003>.
- [20] J.L. Rose, M.J. Avioli, P. Mudge, R. Sanderson, Guided wave inspection potential of defects in rail, in, *NDT and E Int.* (2004) 153–161, <https://doi.org/10.1016/j.ndteint.2003.04.001>.
- [21] P. Rizzo, F.L. di Scalea, Feature extraction for defect detection in strands by guided ultrasonic waves, *Struct. Health Monit.* 5 (2006) 297–308, <https://doi.org/10.1177/1475921706067742>.
- [22] M. Evans, A. Lucas, I. Ingram, The inspection of level crossing rails using guided waves, *Constr. Build. Mater.* 179 (2018) 614–618, <https://doi.org/10.1016/j.conbuildmat.2018.05.178>.
- [23] P. Hu, H. Wang, G. Tian, Y. Liu, X. Li, B.F. Spencer, Multifunctional flexible sensor array-based damage monitoring for switch rail using passive and active sensing, *Smart Mater. Struct.* 29 (9) (2020) 095013.
- [24] H. Sun, L. Peng, S. Huang, Q. Wang, S. Wang, W. Zhao, Analytical model and optimal focal position selection for oblique point-focusing shear horizontal guided wave EMAT, *Constr. Build. Mater.* 258 (2020) 120375.
- [25] C.M. Lee, J.L. Rose, Y. Cho, A guided wave approach to defect detection under shelling in rail, *NDT and E Int.* 42 (3) (2009) 174–180.
- [26] B. Masserey, P. Fromme, Fatigue crack growth monitoring using high-frequency guided waves, *Struct. Health Monit.* 12 (2013) 484–493, <https://doi.org/10.1177/1475921713498532>.
- [27] P. Cawley, M. Lowe, D. Alleyne, et al., Practical long range guided wave testing: Applications to pipes and rail, *Mater. Eval.* 61 (2003) 66–74.
- [28] P. Wilcox, M. Evans, B. Pavlakovic, D. Alleyne, K. Vine, P. Cawley, M. Lowe, Guided wave testing of rail, *Insight- Non-Destructive Testing and Condition Monitoring* 45 (6) (2003) 413–420.
- [29] F. Yuan, Y. Yu, B. Liu, et al., Investigation on optimal detection position of DC electromagnetic NDT in crack characterization for high-speed rail track, 2019 IEEE International Instrumentation and Measurement Technology Conference (I2MTC). IEEE, 2019. <https://doi.org/10.1109/I2MTC.2019.8827153>.
- [30] R. Sanderson, The application of finite element modelling to guided ultrasonic waves in rails Advances in Resolution and Sensitivity of Ultrasonic Guided Waves View project Development and maintenance of BS 7910 View project, 2002. <https://www.researchgate.net/publication/279902853>.
- [31] Y. Gharaibeh, R. Sanderson, P. Mudge, C. Ennaceur, W. Balachandran, Investigation of the behaviour of selected ultrasonic guided wave modes to inspect rails for long-range testing and monitoring, *Proc. Inst. Mech. Eng. F J. Rail Rapid. Transit.* 225 (2011) 311–324, <https://doi.org/10.1243/09544097JRRT413>.
- [32] B. Ndiwe, P. KAh, Njock Bayock, et al., Numerical and experimental investigations of mechanical properties of AW 6005-T6 Aluminium alloy butt weld joint using GMAW process, *Metall. Mater. Eng.* 29 (2023), 16–36. <https://doi.org/10.56801/MME907>.
- [33] G. Velidi, Pressure and velocity variation in remote-controlled plane using CFD analysis, *J. Airline Oper. Aviation Manage.* 1 (2022) 9–18. <https://doi.org/10.56801/1/jaoam.v1i1.2>.
- [34] J. Matsushima, M. Ali, F. Bouchaala, Propagation of waves with a wide range of frequencies in digital core samples and dynamic strain anomaly detection: carbonate rock as a case study, *Geophys. J. Int.* 224 (2022) 340–354.
- [35] L. Yizhi, Z. Xiangming, Image processing and flow field reconstruction algorithm of fluid trajectory in pipeline, *Rev. Adhesion and Adhesives* 10 (2022).
- [36] T. Wei, Dynamic numerical simulation of competitive aerobics based on computational fluid dynamics, *Rev. Adhesion Adhesives* 9 (2021).
- [37] F. Bouchaala, M.Y. Ali, J. Matsushima, Y. Bouzidi, M.S. Jouini, E.M. Takougang, A. A. Mohamed, Estimation of seismic wave attenuation from 3d seismic data: A case study of OBC data acquired in an offshore oilfield, *Energies* 15 (2) (2022) 534.
- [38] P. Brown, P. Mazumder, Current progress in mechanically durable water-repellent surfaces: A critical review, *Rev. Adhesion Adhesives* 9 (2021) 123–152.
- [39] A. Bhosale, S. Patil, V. Dhepe, K. Banosde, R. Kakde, R. Teltumade, D. Lengare, 3-D Numerical study of effect of urea injector location and intake cone geometry on scr performance, *Int. J. Innovative Res. Sci. Stud.* 5 (2) (2022) 47–58.
- [40] C. Yang, K. Kaynarda, S. Salamone, Investigation of wave propagation and attenuation in periodic supported rails using wave finite element method, *Acta Mech.* (2023), <https://doi.org/10.1007/s00707-023-03484-8>.
- [41] P. Xu, H. Zeng, T. Qian, L. Liu, Research on defect detection of high-speed rail based on multi-frequency excitation composite electromagnetic method, *Measurement* 187 (2022) 110351.
- [42] G. Zumpano, M. Meo, A new damage detection technique based on wave propagation for rails, *Int. J. Solids Struct.* 43 (2006) 1023–1046, <https://doi.org/10.1016/j.ijsolstr.2005.05.006>.
- [43] P. Xu, C.L. Zhu, H.M. Zeng, P. Wang, Rail crack detection and evaluation at high speed based on differential ECT system, *Measurement (Lond.)* 166 (2020) 108152.
- [44] S. Hu, W. Shi, C. Lu, Y. Chen, G. Chen, G. Shen, Rapid detection of cracks in the rail foot by ultrasonic B-scan imaging using a shear horizontal guided wave electromagnetic acoustic transducer, *NDT and E Int.* 120 (2021) 102437.
- [45] T. Hayashi, W.J. Song, J.L. Rose, Guided wave dispersion curves for a bar with an arbitrary cross-section, a rod and rail example, *Ultrasonics* 41 (2003) 175–183, [https://doi.org/10.1016/S0041-624X\(03\)00097-0](https://doi.org/10.1016/S0041-624X(03)00097-0).
- [46] I.I. Setschedi, P.W. Loveday, C.S. Long, D.N. Wilke, Estimation of rail properties using semi-analytical finite element models and guided wave ultrasound measurements, *Ultrasonics* 96 (2019) 240–252, <https://doi.org/10.1016/j.ultras.2018.12.015>.
- [47] Y. Wang, C.L. Pasiliao, Modeling ablation of laminated composites: A novel manual mesh moving finite element analysis procedure with ABAQUS, *Int. J. Heat Mass Transf.* 116 (2018) 306–313, <https://doi.org/10.1016/j.ijheatmasstransfer.2017.09.038>.
- [48] W. Zhang, E.E. Seylabi, E. Taciroglu, An ABAQUS toolbox for soil-structure interaction analysis, *Comput. Geotech.* 114 (2019) 103143.
- [49] J. Shen, M. Liu, C. Dong, Z. Meng, G. Liu, H. Cai, L. Zhou, C. Davis, Analysis on asymmetrical RCF cracks characterisation using an ACF-M sensor and the influence of the rail head profile, *Measurement* 194 (2022) 111008.
- [50] I. Bartoli, F. Lanza Di Scalea, M. Fateh, E. Viola, Modeling guided wave propagation with application to the long-range defect detection in railroad tracks, *NDT and E Int.* 38 (2005) 325–334, <https://doi.org/10.1016/j.ndteint.2004.10.008>.
- [51] D. Hesse, P. Cawley, Surface wave modes in rails, *J. Acoust. Soc. Am.* 120 (2006) 733–740, <https://doi.org/10.1121/1.2211587>.
- [52] J. Wu, Z. Tang, F. Lü, K. Yang, Ultrasonic guided wave focusing in waveguides with constant irregular cross-sections, *Ultrasonics* 89 (2018) 1–12, <https://doi.org/10.1016/j.ultras.2018.04.003>.
- [53] A. Cavuto, M. Martarelli, G. Pandarese, G.M. Revel, E.P. Tomasini, FEM based design of experiments for train wheelset diagnostics by laser ultrasonics, *Ultrasonics* 113 (2021) 106368.
- [54] L. Cohen, P. Loughlin, leID1. Time-frequency analysis: Theory and applications, *J. Acoust. Soc. Am.* 134 (2013), 4002. <https://doi.org/10.1121/1.4830599>.
- [55] M. Fernández-Ros, J.A. Gázquez Parra, R.M. García Salvador, N.N. Castellano, Optimization of the periodogram average for the estimation of the power spectral density (PSD) of weak signals in the ELF band, *Measurement (Lond)* 78 (2016) 207–218, <https://doi.org/10.1016/j.measurement.2015.10.006>.
- [56] H. Nakhlé Mahal, K. Yang, A. Nandi, Defect detection using power spectrum of torsional waves in guided-wave inspection of pipelines, *Appl. Sci. (Switzerland)* 9 (7) (2019) 1449.